UPPSALA
UNIVERSITET

Surface Coatings as Xenon Diffusion Barriers for Improved Detection of Clandestine Nuclear Explosions

LISA BLÄCKBERG

Dissertation presented at Uppsala University to be publicly examined in 80121, Ångströmlaboratoriet, Lägerhyddsvägen 1, Uppsala, Friday, 28 February 2014 at 10:15 for the degree of Doctor of Philosophy. The examination will be conducted in English. Faculty examiner: Prof. Kai Vetter (UC Berkeley, CA, USA, Department of Nuclear Engineering).

Abstract
Bläckberg, L. 2014. Surface Coatings as Xenon Diffusion Barriers for Improved Detection of Clandestine Nuclear Explosions. *Digital Comprehensive Summaries of Uppsala Dissertations from the Faculty of Science and Technology* 1111. 94 pp. Uppsala: Acta Universitatis Upsaliensis. ISBN 978-91-554-8848-2.

This thesis investigates surface coatings as xenon diffusion barriers on plastic scintillators. The motivation for the work is improved radioxenon detection systems, used within the verification regime of the Comprehensive Nuclear-Test-Ban Treaty (CTBT).

One type of radioxenon detection systems used in this context is the Swedish SAUNA system. This system uses a cylindrical plastic scintillator cell to measure the beta decay from radioxenon isotopes. The detector cell also acts as a container for the xenon sample during the measurement.

One problem with this setup is that part of the xenon sample diffuses into the plastic scintillator material during the measurement, resulting in residual activity left in the detector during subsequent measurements. This residual activity is here referred to as the memory effect.

It is here proposed, and demonstrated, that it is possible to coat the plastic scintillator material with a transparent oxide coating, working as a xenon diffusion barrier. It is found that a 425 nm Al_2O_3 coating, deposited with Atomic Layer Deposition, reduces the memory effect by a factor of 1000, compared an uncoated detector. Furthermore, simulations show that the coating might also improve the light collection in the detector. Finally, the energy resolution of a coated detector is studied, and no degradation is observed.

The focus of the thesis is measurements of the diffusion barrier properties of Al_2O_3 films of different thicknesses deposited on plastic scintillators, as well as an evaluation of the expected effect of a coating on the energy resolution of the detector. The latter is studied through light transport simulations. As a final step, a complete coated plastic scintillator cell is evaluated in terms of memory effect, efficiency and energy resolution.

In addition, the xenon diffusion process in the plastic material is studied, and molecular dynamics simulations of the Xe-Al_2O_3 system are performed in order to investigate the reason for the need for a rather thick coating to significantly reduce the memory effect.

Keywords: Radioxenon, Gas Diffusion Barrier, Plastic Scintillator, Comprehensive Nuclear-Test-Ban Treaty, Atomic Layer Deposition, Al_2O_3, Molecular Dynamics, Light Transport

Lisa Bläckberg, Department of Physics and Astronomy, Materials Theory, Box 516, Uppsala University, SE-751 20 Uppsala, Sweden.

Till P och S

List of papers

This thesis is based on the following papers, which are referred to in the text by their Roman numerals.

I **L. Bläckberg**, A. Fay, S. Biegalski, M. Boman, K. Elmgren, T. Fritioff, A. Johansson, L. Mårtensson, F. Nielsen, A. Ringbom, M. Rooth, H. Sjöstrand and M. Klintenberg
Investigations of surface coatings to reduce memory effect in plastic scintillator detectors used for radioxenon detection
Nuclear Instruments and Methods in Physics Research A **656** 84-91 (2011)

II **L. Bläckberg**, M. Klintenberg, A. Ringbom and H. Sjöstrand
Effects of surface coatings on the light collection in plastic scintillators used for radioxenon detection
Physica Scripta **T150** 014007 (2012)

III **L. Bläckberg**, T. Fritioff, L. Mårtensson, F. Nielsen, A. Ringbom, H. Sjöstrand and M. Klintenberg
Memory effect, resolution, and efficiency measurements of an Al_2O_3 coated plastic scintillator used for radioxenon detection
Nuclear Instruments and Methods in Physics Research A **714** 128-135 (2013)

IV **L. Bläckberg**, A. Ringbom, H. Sjöstrand and M. Klintenberg
Assisted self-healing in ripped graphene
Physical Review B **82** 195434 (2010)

V **L. Bläckberg**, E. Metsanurk, A. Tamm, A. Aabloo and M. Klintenberg
Molecular dynamics study of Xenon on an amorphous Al_2O_3 surface
Submitted to Nuclear Instruments and Methods in Physics Research A (January 2014)

Reprints were made with permission from the publishers.

Contents

1. Introduction

The main subject of this thesis is radiation detection, and more specifically, improvements of the SAUNA system (Swedish Automatic Unit for Noble gas Acquisition), which is used to detect radioactive xenon in the atmosphere in order to discover clandestine nuclear test explosions for verification of compliance with the Comprehensive Nuclear-Test-Ban Treaty (CTBT).

The system uses a plastic scintillator detector to measure the radiation emitted from the xenon isotopes to be detected. An issue with this setup is that part of the xenon sample, diffuses into the detector material during the measurement, resulting in an unwanted memory effect. The residual activity in the detector impairs the sensitivity of the system and complicates the measurement procedure, as well as maintenance of the system.

The work presented in this thesis is dedicated to removing or reducing this memory effect, and the main approach investigated to do this is to coat the plastic scintillator detector with a material that is acting as a xenon diffusion barrier, without impairing the performance of the detector. In this work Al_2O_3 deposited with low temperature Atomic Layer Deposition (ALD) is identified as a suitable coating material for this application.

This first chapter intends to give an overview of the field of radiation detection and contains a brief introduction to what radioactivity and radiation is, and how these phenomena can be measured and characterized. Emphasis will be given to the types of radiation, and type of detectors, studied in the work described in the remainder of this thesis.

Chapter 2 discusses nuclear disarmament, non-proliferation treaties and the verification regime of the CTBT, in order to give a background to the purpose of these specific radioxenon detection systems.

In Chapter 3 the procedures used to detect atmospheric radioxenon are discussed, as well as the memory effect problem. Potential solutions to the problem are also proposed, with emphasis given to the coating approach.

Chapter 4 describes a study performed in order to better understand the mechanisms behind the memory effect.

The evaluation of the coating approach, with focus on Al_2O_3, is summarized in Chapter 5, which is based on Papers I-IV included in this thesis.

In Chapter 6 a theoretical study of xenon interactions with Al_2O_3 surfaces is described, in order to better understand the performance of the coating material. This chapter is based on Paper V.

Finally, Chapter 7 contains the conclusions of the thesis.

1.1 Radioactivity

When a nucleus is found in an unstable state, it will eventually decay to a stable state, and in this process emit its excess energy in the form of radiation. Such unstable nuclei are radioactive [1].

The decay process is statistical in nature, and it is impossible to predict when a certain nucleus will decay. The decay is however characterized by the half life, $t_{1/2}$, which is the time needed for half of the nuclei in a sample to decay. The half life is characteristic of each type of radioactive isotope.

The activity A of a sample is defined as the number of decays per unit time, and it is related to the number of radioactive nuclei N in a sample by the following equation:

$$A(t) = \left| \frac{dN}{dt} \right| = \lambda N(t) = \lambda N_0 e^{-\lambda t} = A_0 e^{-\lambda t}, \tag{1.1}$$

where λ is the decay constant given by $\lambda = \frac{ln(2)}{t_{1/2}}$, and N_0 and A_0 are the number of nuclei, and the activity of the sample at $t = 0$, respectively. By measuring the radiation emitted from a sample, one can thus calculate the activity, and number of radioactive nuclei in the sample [1].

1.2 Types of ionizing radiation

Ionizing radiation is composed of particles that carry enough energy to ionize atoms in a material they pass through. The minimum ionization energy is typically around 10 eV.

Due to the difference with which different kinds of radiation interact with matter, it is common to talk about *charged* and *neutral* radiation separately. In the following sections the characteristics of these two types of radiation, as well as their possible origins and modes of interaction with matter will be discussed. This description is not intended to be complete, but rather to cover the types of radiation, decay modes, and interactions that will be discussed in the remainder of this thesis.

1.2.1 Charged radiation

There are two general types of charged radiation, heavy charged particles and fast electrons/positrons. Heavy charged particles refer to all energetic ions such as protons, alpha particles and fission products.

A few origins of fast electrons will be described in the following paragraphs.

Beta-decay

The net effect of beta-decay is that a neutron in the nucleus of the atom is converted to a proton, or the other way around. To conserve electric charge a positive or negative beta particle ($\beta^{\pm}$) is emitted in the process, together with a neutrino (ν) or an antineutrino ($\bar{\nu}$). The process can be described using the following equation:

$$\, ^A_Z X \rightarrow \, ^A_{Z\pm1} Y + \beta^{\mp} + \bar{\nu}/\nu, \tag{1.2}$$

where X is the original parent nucleus, and Y is the daughter nucleus resulting from the decay. It should be noted that the beta-decay changes the atomic number of the nucleus, and the daughter nucleus is thus not the same element as the parent nucleus.

The recoil energy of the daughter nucleus Y is usually extremely small so the energy released by the beta decay is essentially shared between the beta particle and the (undetectable) neutrino. The energy of the emitted beta-particle can be anything between 0 and an endpoint energy Q_β which corresponds to the energy difference between the initial and final nuclear states. A spectrum of beta particles from a particular beta decay is thus continuous in energy between 0 and Q_β [1].

Internal Conversion

An excited nucleus can go back to its fundamental state through internal conversion. In this process the excitation energy of the nucleus is transferred to an orbital electron which can be ejected from the atom. The energy of the emitted electron, called a conversion electron (CE), is given by the difference in excitation energy E_{ex} and the binding energy of the electron E_b:

$$E(CE) = E_{ex} - E_b \tag{1.3}$$

Internal conversion thus causes a discrete energy spectrum, characteristic of the binding energies and excitation energies, rather than a continuous one as in the case of beta decay. However, for a certain isotope, the ejected electron may originate from different shells with different binding energies which causes several discrete electron energies in the resulting spectrum [2].

1.2.2 Neutral radiation

Neutral radiation consists of particles without charge such as photons (electromagnetic radiation) and neutrons. Neutrons are generated in various nuclear processes such as fission and reactions including heavy charged particles [2]. The photons can be for example X-rays from atomic transitions or gamma rays from nuclear transitions.

Gamma rays

An excited nucleus can release its excess energy by emitting a gamma ray, carrying the full excitation energy. It is quite common that a beta decay leaves the daughter nucleus in an excited sate, resulting in a gamma emission following the beta decay. This is the case for two of the xenon isotopes detected by the SAUNA system as explained in Section 3.1.1.

X-rays

When gamma rays are emitted in nuclear transitions, X-rays are emitted in atomic transitions due to rearrangement of electrons. These X-rays are characteristic of every element, and their discrete energies correspond to the difference in binding energies between the electronic shells. The excited atomic states can be reached by a number of processes, like electron capture by the nucleus, internal conversion or excitation by external radiation [2].

X-rays can also be emitted as so called bremsstrahlung when fast electrons are deflected by the charged nuclei in a material, resulting in a continuous X-ray spectrum. The X-ray energies are lower than typical gamma ray energies.

1.3 Radiation interaction with materials

To understand how a radiation detector works, one needs to understand how different types of radiation interact with matter. The idea of radiation detection is to study the trace that the radiation leaves in the detector, which depends on how it interacts with the detector material. One great distinction between charged and neutral radiation is the nature of these interactions.

Charged radiation will continuously lose energy while passing through the detector material due to Coulomb interactions with the charged nuclei and electrons in the material.

Uncharged particles on the other hand, loses energy due to discrete events. In these events secondary charged radiation can be created, and in turn gradually deposit their energy. Neutrons can induce nuclear reactions ((n,p), (n,α) etc.) or get scattered, resulting in recoil nuclei as secondary charged radiation, while the secondary charged radiation of photons is fast electrons. Due to the discrete nature of the energy loss of uncharged radiation, a neutron or a photon may pass through a material without leaving a single trace [2].

The remainder of this section will focus on the interactions of fast electrons and photons, since these are the kinds of radiation that are emitted by the xenon isotopes measured by the SAUNA system.

1.3.1 Fast electrons

Fast electrons can lose energy, and be deflected, in two ways when passing through a material, either through collisional losses, or radiative losses.

Collisional losses occur due to Coulomb forces between the incoming electron and the orbital electrons and nuclei in the material, and results in ionization or excitation of the atoms in the absorber material.

The radiative losses occur since any charge irradiates energy when it is accelerated. The deflections of the fast electrons due to the encounters with orbital electrons and nuclei causes acceleration of the incoming fast electrons, and the energy is irradiated as bremsstrahlung, as described in Section 1.2.2.

For electrons with energies less than a few MeV, the collisional losses dominate, and it is only for materials with very high atomic number that the radiative losses are significant [2]. For electrons of higher energy, the radiative losses become more important.

In Ref. [3] specific energy losses (collisional, radiative, and total) are tabulated as a function of electron energy for a large number of absorber materials. Complete expressions for both types of losses can be found in Ref. [4].

1.3.2 Photons

Photons interact with matter and lose their energy through three main processes: photoelectric absorption, Compton scattering and pair production. Often the same photon can undergo various of these interactions before all of its energy is lost in the material [2].

The preferred interaction in radiation detectors is photoelectric absorption since in this process the full photon energy is deposited in one single event.

Photoelectric absorption

In photoelectric absorption the energy of the photon is completely absorbed by an atom. One of the electrons, usually from the inner shell of the atom, is then ejected as a so called photoelectron. The energy of the photoelectron corresponds to the difference between the energy of the incident photon, and the binding energy of the electron: $E_{pe} = h\nu - E_b$. The complete energy of a photon cannot be absorbed by a free electron since the atom is needed for conservation of momentum [1].

Photoelectric absorption is the dominant process for low photon energies and in materials with high atomic number Z. The probability of the process decreases rapidly with increasing photon energy.

Compton scattering

Compton scattering is an inelastic collision between the photon and a nearly free atomic electron in the material. For outer shell electrons the binding energy is small compared to the energy of the incoming photon, and may be considered as free and at rest. When encountering the nearly free electron the photon will scatter and transfer part of its energy to this electron. The energy of the scattered photon depends on the energy of the initial photon, and on the scattering angle.

Compton scattering is the predominant process for photons of intermediate energy, and its probability decreases with increasing photon energy. Its probability increases linearly with the atomic number Z of the material.

Pair production

Pair production is the dominant process at high photon energies. It can only occur if the energy of the incident photon is at least 1.02 MeV. In this process the photon energy is completely absorbed and converted to an electron-positron pair. Both these secondary charged particles will slow down in the material and the positron will eventually annihilate with an electron and two 0.511 MeV annihilation photons will be created as by products. The probability of pair production increases with increasing photon energy, and with increasing Z of the absorber.

1.4 Basic description of radiation detection

The net result of radiation interactions in many detectors is the appearance of charge induced within the active volume of the detector. This charge can be collected by applying an electric field over the detector volume. Positive charges will then be drawn to one side of the detector, and negative charge to the other side. This movement of charges constitute the current which forms the basic electric signal from the detector.

If one looks at one quantum of radiation that deposits its energy in the detector, a charge Q will appear as the result of the interaction of the radiation with the detector material. The amount of charge generated depends on the energy of the incoming radiation. The charge can form a current $i(t)$, and the time integral of this current corresponds to the deposited charge:

$$\int_0^{t_c} i(t)dt = Q, \qquad (1.4)$$

where t_c is the collection time, which is the time needed to collect all of the charge Q.

Detectors can be operated in a number of ways, of which the so called pulse mode is the most common.

These detectors record each individual quantum of radiation. The pulses formed correspond to the time integral of the current, which, as shown in equation 1.4, corresponds to the charge Q. Since the generated charge Q depends on the energy E deposited in the detector, one can in this way get information about the energy of each quantum of radiation.

The output of the system is a series of pulses, with pulse heights (i. e. Q values) reflecting the energy of each detected radiation quanta, or particle.

The timing of the pulses gives timing information also of the incoming radiation. The intensity of the radioactive source is related to the frequency of

the pulses. Finally, the type of radiation may be identified from the shapes of the pulses.

The most common way of presenting the output from a pulse mode detector is in a pulse height spectrum. This is a histogram showing number of pulses as a function of Q. By using sources with known energy, it is then possible to calibrate the energy scale [2].

1.4.1 Properties

There are various properties that are important for the operation of a radiation detector. The optimal detector should, among other things, be efficient in the conversion of the radiation energy to electric pulses, and it should be able to distinguish radiation of different energies and types. It should also have a fast response, compared to the count rate of the incoming radiation, in order to minimize the system dead time.

In the work presented in this thesis, a major concern has been that coating the SAUNA detector should not impair its energy resolution or efficiency. In this section these properties, as well as the dead time, will be discussed.

Energy resolution

The energy resolution reflects the spread in the pulse height generated by the detector as response to a particle of certain type and energy [4]. The resolution thus determines the ability of the detector to distinguish between particles of different energies.

As will be discussed in Chapter 5, a large part of the work in this thesis has been dedicated to investigate the impact a coating would have on the energy resolution of the detector, since this property is an important factor in the performance of the SAUNA system.

Ideally, the response to identical particles would always be the same, and the spectrum generated by a mono energetic source would be a sharp spike. Such ideal situation is unfortunately not possible to achieve in reality. The reason is that all detectors present some degree of statistical fluctuations in the number of charge carriers produced as a response to a specific particle with a specific energy.

These fluctuations can be assumed to follow Poisson statistics, meaning that the number of charge carriers created in response to a certain particle energy varies around its mean value N_{cc}. The variations are characterized by a standard deviation given by $\sigma = \sqrt{N_{cc}}$.

The resolution R of the detector, for a certain energy, can be defined as:
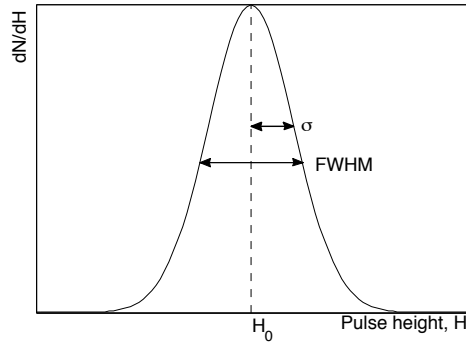
$$R = \frac{FWHM}{H_0} \tag{1.5}$$

Figure 1.1. Pulse heigh spectrum illustrating the definition of the FWHM.

where H_0 is the average pulse height and $FWHM$ is the Full Width Half Maximum, which is defined as the width of the peak at the level defined by half the peak maximum, see Figure 1.1.

If the only contribution to the peak broadening is the fluctuations in the number of charge carriers created, the resulting peak in the pulse height spectrum would have a Gaussian shape (since the mean number of charge carriers N_{cc} is generally a large number, and the Poisson distribution then tends to a Gaussian one). Assuming that the pulse height is linearly dependent on the number of charge carriers created, which is not completely true, but often a good approximation, the resulting resolution is given by:

$$R = \frac{2.35\sqrt{N_{cc}}}{N_{cc}} = \frac{2.35}{\sqrt{N_{cc}}} \qquad (1.6)$$

The energy resolution of a detection system is thus limited by the number of charge carriers. A good energy resolution is characterized by a low value of R, which is achieved if the number of charge carriers is large.

In addition to the statistical fluctuations, there are generally also other sources of fluctuations such as non-uniform response over the active volume of the detector, drifts in the operating parameters and electronic noise, resulting in additional peak broadening. If there are various contributions to the broadening of the peak, and if these are symmetrical and independent, the shape of the peak tends to be Gaussian with a $FWHM_{total}$ defined by:

$$FWHM_{total}^2 = FWHM_1^2 + FWHM_2^2 + FWHM_3^2... \qquad (1.7)$$

where $FWHM_i$ corresponds to the contribution i.

Different contributions to the peak broadening in scintillators are discussed further in Section 1.5.3.

16

Detection efficiency

There are various definitions of detection efficiency.

The absolute efficiency ε_{abs} is the ratio between the number of pulses recorded by the detector and the number of radiation quanta emitted from the source.

The intrinsic efficiency ε_{int} is the ratio between the number of recorded pulses and the number of radiation quanta incident on the detector. The intrinsic efficiency thus take into account only the response of the detector itself, while the absolute efficiency also take into account the geometry of the detector relative to the source of radiation.

For isotropic sources, $\varepsilon_{int} = \varepsilon_{abs}(4\pi/\Omega)$, where Ω is the solid angle of the detector seen by the source.

The effect a coating would have on the detection efficiency of the SAUNA system would be determined by the amount of energy absorbed in the coating before the radiation reaches the active volume of the detector. These losses are however assumed to be small given that the achieved coating is thin, as discussed in Paper I, III, and IV.

Dead time

For all detection systems there is a minimum time interval between two events in the detector where they can be distinguished as two separate pulses. This minimum time is called the dead time τ, and it puts a limit on the time resolution of the detection system. Since radioactive decay is a statistical process, there is always some probability that two events occur within this time interval, and therefore will be lost for detection. For hight count rates this can become a significant problem, which one especially needs to take into account and compensate for if the true count rate of the source is of interest.

The SAUNA system is designed to measure very low activities of diluted radioxenon releases, and dead time is generally not an issue in these systems. However, in experiments described in Chapter 5, and Papers I and III, higher activities were measured and the dead time important to account for.

1.5 Scintillators

The type of detectors that are used in the work presented in this thesis are scintillators. Scintillators are characterized by their ability to reemit the energy absorbed in the detector material in the form of light, a process called fluorescence. The emitted light is transmitted through the detector medium and reflected at surfaces, until it reaches some kind of photosensor where it can be converted to an electrical signal. Sometimes the coupling between the photosensor and the scintillator is aided by transparent light guides [4]. In scintillators the charge carriers are thus not created directly in the detector material, but in a second step after the conversion of light to photoelectrons.

Common light converters are photomultiplier tubes (PM-tubes). In these devices the scintillator light hits a photocathode where the absorption of the photons results in the ejection of photoelectrons. The photoelectrons are accelerated and multiplied by striking a series of electrodes, and the electric signal is amplified. Ideally the output is proportional to the amount of incoming light. PM-tubes are generally most efficient for light in the visible range.

A good scintillator should have a high scintillation efficiency (i. e. produce as large amount of photons as possible for a given incoming radiation energy), and be transparent to the wavelengths of its own emission [5]. It is also important that a good optical match to the PM-tube is achieved, meaning that the refractive index of the scintillator material should be close to the one of the glass window in the PM-tube, to avoid light losses at the interface [4].

Scintillators are generally divided into two groups, depending on their material compositions; organic and inorganic scintillators. Both these types are important for this work, but the work focus on organic scintillators of plastic type, which are used to detect fast electrons in the SAUNA system.

In both types of scintillators the emission of scintillation light takes place by de-excitation through transitions in the electronic structure in the detector material. All non-radiative processes, that compete with the fluorescence, such as conversion of the excitation energy to heat, results in a lower light yield from the scintillator. This is called quenching and can be caused by for example impurities.

The light yield is the number of photons created in the detector as a response to radiation of a specific energy.

1.5.1 Organic scintillators

In organic scintillators light is emitted in transitions between energy levels in the electronic structure of organic molecules. Organic scintillators are mainly composed of carbon and hydrogen, and thus have a low effective atomic number Z, which results in low probability for all three photon interactions described in Section 1.3.2. Therefore it is not common to use organic scintillators for photon detection. They are however often used for detection of other types of radiation (fast electrons, heavy charged particles, and neutrons).

Organic scintillators can either be pure organic crystals, or the scintillating molecules can be solved in a liquid or plastic. Plastic scintillators are widely used since they are easy to manufacture in different shapes and sizes [4].

In the case of liquid and plastic scintillators, the conversion of radiation energy to scintillator light is a three step process (for pure crystals the second step is omitted).

First the energy of the incident radiation is absorbed, mainly by the solvent molecules since they constitute the major fraction of the material. Secondly the excitation energy migrates to the scintillating organic molecules, which de-

excite and emit photons in the third step. The energy of the emitted photons is determined by the difference in energy between the excited and ground states of the molecules. The organic molecules are normally chosen such that this energy corresponds to visible light.

Sometimes an additional constituent is added to the solution, acting as a wavelength shifter. These molecules absorb the scintillator light and re-emit it at a different wavelength. This can be useful to match the light with the highest sensitivity of the PM-tubes.

1.5.2 Inorganic scintillators

Inorganic scintillators rely on a crystal structure of the material for the scintillation process to take place. The effect of radiation incident on an inorganic crystal is that electrons are elevated from the valence band to the conduction band. The result is the formation of so called electron-hole pairs, each consisting of an extra electron in the conduction band, and a vacancy in the valence band. The de-excitation, resulting in the emission of scintillator photons, occur when these electron-hole pairs recombine.

Inorganic scintillators can either be self activated, or they can be doped. In self activated scintillators the recombination takes place by the electron jumping from the bottom of the conduction band to the top of the valence band, and the energy of the emitted photon will correspond to the band gap of the crystal.
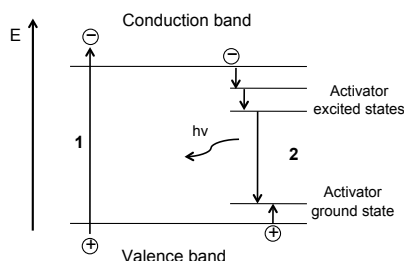
Figure 1.2. Schematic picture of the scintillation process in an activated inorganic crystal. In step 1 an electron is excited to the conduction band, leaving a hole in the valence band. In step 2 the electron-hole pair migrates to an activator site, where the hole ionizes the activator. The electron then recombines with the hole with the emission of a photon. The energy of the photon is characterized by the energy levels of the activator, and is lower than the full band gap of the crystal.

In doped (activated) scintillators, impurities are introduced into the host crystal. These impurities can have energy levels within the band gap of the crystal, offering an alternative way for de-excitation, resulting in the emission of photons with an energy level lower than the full band gap of the crystal

(see Figure 1.2). The composition of the crystal and the choice of activators can be tailored such that the emitted photons are in the visible range, which is desirable for good coupling to the PM-tubes.

1.5.3 Energy resolution of scintillators

Scintillators have relatively poor energy resolution, and therefore broad peaks compared to high resolution detectors, such as semiconductor detectors.

In most cases the dominant contribution to the peak broadening in scintillators is the photoelectron statistics, which is determined by the number of photoelectrons created at the photocathode as a result of the interaction of radiation within the detector.

The number of photoelectrons $N_{photoel}$ created at the photocathode depends on:

- The number of scintillator photons N_γ created in the detector as a response to a radiation quantum of a certain energy. This is defined as the light yield of the detector.
- The light collection efficiency ε_{coll} of the detector, which is equal to the fraction of all created photons that reach the photocathode of the PM-tube.
- The quantum efficiency ζ of the PM-tube which is the ratio between the number of photoelectrons created and the number of photons incident on the photocathode.

The mean number of photoelectrons created as a response to a certain particle energy can be expressed as $N_{photoel} = N_{scint}\varepsilon_{coll}\zeta$. The statistical variance in the number of created photoelectrons is, according to poisson statistics, given by $\sigma = \sqrt{N_{photoel}}$ (as explained also in Section 1.4.1), and the relative variance thus decreases with an increased number of photoelectrons.

The main additional contributions to the peak broadening in scintillators are:

- Variations in response over the active volume of the detector. These variations are usually dominated by non-uniform light collection efficiency, and a spread in the number of photons reaching the PM-tube depending on where in the detector the interaction took place, will add to the peak broadening. This non-uniformity can be a significant contribution for large detectors, or detectors with complex shape.
- Electronic noise in the components used in the detector system.
- Drifts in operating parameters during the course of the measurement. For scintillator detector systems these drifts are usually related to the PM-tubes.

The different contributions may be added according to Equation 1.7 in order to obtain the overall resolution of a scintillator detection system.

Light collection

For the SAUNA plastic scintillator detector, which is shaped as a cylindrical hollow cell, the photoelectron statistics and the spatial variations in detector response are assumed to be the dominant contributions to the energy resolution, as is further discussed in Chapter 5. Since both the photoelectron statistics and the spatial variations are governed by the light collection in the detector, the latter is an important factor to consider.

A less than perfect light collection can be due to self absorption in the scintillator material, or losses at the surfaces of the material.

Self absorption can be caused by overlapping absorption and emission spectra, impurities in the material or inherent absorption in the solvent (in the case of organic scintillators) [6]. Losses due to self absorption are usually only significant for large scintillators.

Since light is emitted in all angles in a scintillation event, part of the created light will inevitably undergo surface interactions before reaching the PM-tubes. When light hits a surface it can either be reflected back into the material it came from, or it can be transmitted into the adjacent medium. If the incident angle is larger than a certain critical angle, total internal reflection occurs. If the incident angle is smaller than the critical angle part of the light is reflected, and part is transmitted into the adjacent medium, according to Fresnels formula [4]. The critical angle θ_c is determined from Snell's law of refraction to:

$$\theta_c = \sin^{-1} \frac{n_2}{n_1}, \tag{1.8}$$

where n_1 and n_2 are the refractive indices of the scintillator and the adjacent medium, respectively. In order to increase the light collection efficiency an external reflector is often used to recapture some of the transmitted light. The reflector can be either specular or diffuse, but it has been shown that a diffuse reflector is often to prefer, since these spread the light in arbitrary angles, and the risk of the light being trapped by multiple internal reflections is smaller. There are various different external reflectors used, like white paint, aluminum foil, and teflon tape.

To avoid reflection at the interface between the scintillator and the photocathode of the PM-tube, the photocathode often has a glass window with a refractive index similar to those of many scintillators. It is important that there is no gap between the two materials since this will increase the risk of light being reflected back into the scintillator. To solve this problem optical grease, and/or optical pillows with refractive indices close to the one of the scintillator are often used, in order to assure that there is no air between the scintillator and the PM-tube.

It should also be noted that an increased number of surface reflections increase the mean path travelled by the photons, which will make self absorption more significant.

When designing a scintillator detection system it is important to consider how the geometry of the detector may be optimized for good light collection.

2. Background - Nuclear Disarmament

In August 1945, during the final stages of the second world war, the United States dropped two nuclear fission bombs over Japan. The uranium bomb *"Little boy"* exploded over Hiroshima on August 6, and 3 days later the plutonium bomb *"Fat man"* was dropped over Nagasaki. The use of the nuclear bombs resulted in the death of 210 000 people directly at the time of the explosions and during the following months, and 130 000 more died within 5 years after the events due to radiation exposure [7].

After these events the work of preventing more countries from acquiring the extremely powerful nuclear weapons began, and at the same time work was conducted to spread knowledge and technology for peaceful nuclear energy. The technology and physics basis is similar for the two applications, which has lead to a need for strict control over nuclear materials and technologies, in order to assure that they are used for the right purpose.

In 1957 the International Atomic Energy Agency (IAEA) was formed, with the purpose of promoting research and development of nuclear technology for peaceful uses, as well as to establish and develop safety standards [8].

2.1 International nuclear-non proliferation treaties

The two-fold nature of nuclear technology has resulted in the establishment of a number of international treaties, in order to aid the peaceful use of the technology, and at the same time preventing the spread and use of nuclear weapons.

PTBT
The Partial Test Ban Treaty (PTBT) bans all nuclear test explosions, except those performed underground. The PTBT entered into force in 1963. This treaty was established to slow down the nuclear arms race, and to stop the nuclear fallout into the atmosphere [9].

NPT
In 1968 the Nuclear Non-Proliferation Treaty (NPT) was opened for signature, and the treaty entered into force 2 years later [10]. The NPT has three purposes. It should prevent the spread of nuclear weapons, promote nuclear disarmament, and promote the peaceful use of nuclear energy.

IAEA was given the responsibility of applying safeguards for verification of compliance with the NPT, and the treaty resulted in that many countries abandoned their nuclear weapons programs.

CTBT

The continuation of the PTBT is the Comprehensive Nuclear-Test-Ban Treaty, CTBT, which bans all nuclear test explosions, also those performed underground. The CTBT was opened for signature in 1996, and it has up until today been signed by 183 states and ratified by 161 [9].

The treaty has not yet entered into force. It will do so 6 months after all 44 so called Annex 2 states have both signed and ratified the treaty. The Annex 2 states are those that in 1996 were on IAEA's list of countries with nuclear research or nuclear reactors. The states missing for entry into force are DPRK, India and Pakistan who have neither signed nor ratified, and USA, China, Iran, Israel and Egypt, who have signed the treaty but not ratified it.

2.2 Nuclear testing historically

Even though nuclear weapons have only been used twice in war, a large number of nuclear test explosions have been performed. Between 1945 and 1996, more than 2000 nuclear tests were performed by USA, Russia, UK, France and China, and one test each by India and Pakistan. Before 1963, when the PTBT entered into force, most of the explosions were atmospheric, however after 1963 most tests have been conducted underground. Since the CTBT opened for signature in 1996 only 6 tests have been conducted; one by India in 1998, two by Pakistan the same year, and three by DPRK in 2006, 2009 and 2013.

2.3 Verification of the CTBT

When the CTBT entries into force there is a need for a verification regime in order to verify the compliance with the treaty. Right now such regime is being constructed by the Comprehensive Nuclear-Test-Ban Treaty Organization (CTBTO) [9]. The verification regime consists of an International Monitoring System (IMS), which, when it is completed, will contain 337 monitoring stations, supported by 16 radionuclide labs, spread over the world as shown in Figure 2.1.

The IMS is designed to detect energy release and radionuclide production, which are two basic phenomena caused by a nuclear explosion. The energy release is monitored using seismic, infrasound, and hydroacoustic measurement systems. Such measurements can give information about the size, time, and location of an explosion.

In order to distinguish a nuclear explosion from a conventional one, it is necessary to also detect radionuclides released in the explosion. This is particularly true for low yield explosions, which are easier to perform with conventional explosives. Radionuclide detection is done using aerosol stations detecting airborne radioactive particles, and noble gas detection systems monitoring
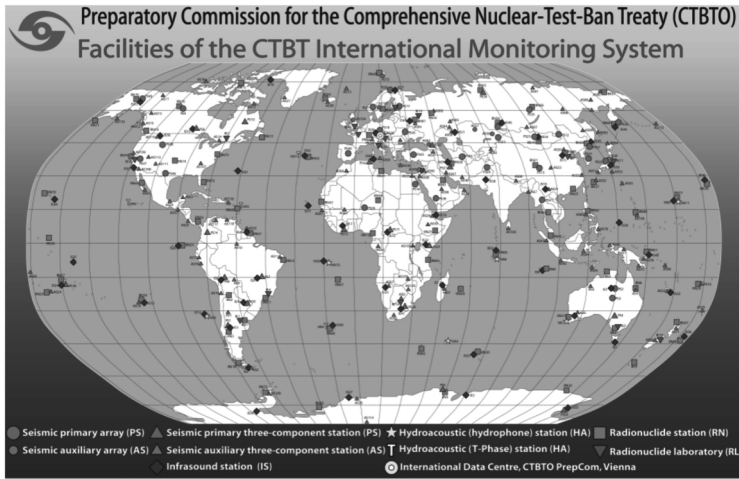
Figure 2.1. The International Monitoring System [9].

radioxenon in the atmosphere. The main topic of this thesis is improvement of these radioxenon detection systems.

Atmospheric Transport Modeling (ATM) is used to backtrack the radioactive plume from its point of detection, in order to see if it is consistent with the explosion site. It can also be used to predict the path of a release from a specific location.

To be able to detect an explosion anywhere on earth many of the IMS stations are located in remote inaccessible areas, which puts great demands on the automatic functioning of the measurement systems. As of January 2014 over 80% of the network is up and running.

Data from all the monitoring stations are continuously being sent via a Global Communication Infrastructure (GCI), to the International Data Center (IDC) located in Vienna, Austria, where it is processed and analyzed. Data is also available to National Data Centers (NDC) in the member states, who are able to perform independent analysis of the data. The Swedish Defence Research Agency (FOI) are responsible for the Swedish NDC, and also operates two IMS stations. One is a seismic station located in Hagfors, and the other one is a radionuclide station in Kista consisting of both a particulate and a noble gas detection system [11].

When the treaty entries into force, CTBTO will also be able to perform On Site Inspections (OSI) when a violation of the treaty is suspected, and the technology to aid such inspections is now being developed [9]. An OSI can be requested by a member state in case of a suspicious event in another member state. The inspection may involve a number of activities, including vi-

sual observations, environmental sampling, radiation monitoring, and seismic measurements.

2.4 Monitoring technologies

As mentioned earlier, the monitoring equipment used in the IMS are divided into 4 modalities; seismic, hydroacoustic, infrasound, and radionuclide measurement stations. The first three modalities are based on waveform analysis, dedicated to detect the energy release from the explosion, taking place underground, underwater, or in the atmosphere. The complementing radionuclide modality is needed to verify the nuclear nature of an explosion [9].

Seismic

The seismic network consist of 170 measurement stations where seismic sensors monitor waves propagating through earth [9]. The waves can originate from, for example, explosions or earthquakes. The purpose of the seismic monitoring is to discover underground nuclear explosions. One advantage of seismic waves is that they travel very fast, and an event can be measured anywhere on earth within 10 minutes after occurring. There are both fast traveling body waves inside the earth, and slower and more destructive surface waves. There are two types of seismic monitoring stations used in the IMS, seismic arrays and three-component sensors. Seismic arrays consist of various sensors spread over a wide area, and three component sensors only contain one sensor and therefore have a larger error, but are cheaper.

Hydroacoustic

Hydroacoustic monitoring stations measure acoustic energy traveling in water. Since water very efficiently transports such energy, it is enough with 11 stations to cover all oceans on earth [9]. Hydroacoustic signals can be used to discover nuclear tests underwater, but also atmospheric and underground tests performed near the ocean surface or near the coast, respectively.

There are two kinds of stations in the IMS measuring hydroacoustic waves. The first type are seismic three-component sensors located on small islands with steep slopes. They measure the acoustic wave as it is transformed into a seismic one upon hitting land. The other type of systems are underwater hydrophones. These consist of microphones located at a depth between 600 and 1200 meters. From the microphones there are cables transferring the signal to an island, which can be located as far as 100 km from the microphones.

Infrasound

The third wave-sensing modality in the IMS is infrasound monitoring. Infrasound consists of acoustic waves with very low frequency, not audible for the human ear [9]. Infrasound can be generated both by natural sources like

volcanoes, earthquakes, and storms, and by man made sources like explosions and rocket launching. The infrasonic waves are detected by sensors measuring micro pressure changes in the atmosphere. There are 60 infrasound stations in the IMS, which can be used to detect atmospheric tests as well as shallow underground explosions.

Radionuclear

The final modality is radionuclide monitoring. This modality is needed to verify if an event picked up by the other 3 monitoring systems, is nuclear in nature or not. The purpose of the radionuclide network is to capture and measure the radioactive debris which is released in the explosion, and spread in the atmosphere by winds. The radioactivity can either be bomb material, fission- or activation products in particulate form, or radioactive gases (mainly noble gases). There are 80 stations monitoring the radioactive particles by sampling air and passing it through a filter which captures a large part of the particles [9]. This filter is exchanged every day, and the radioisotopes it contains are identified and quantified through gamma ray spectroscopy.

40 of the 80 radionuclide stations are to be equipped with additional radioxenon monitoring capabilities. As of January 2014, 30 of the radioxenon monitoring systems are installed. These systems monitor the atmospheric concentration of radioxenon, and will be described in more detail in Chapter 3. Four different radioxenon detection systems have been developed specifically for use in the IMS, within the framework of the International Noble Gas Experiment (INGE) [12]. The INGE collaboration was formed in order to facilitate the development of equipment meeting the specific requirements of use in the IMS. The IMS systems need to be able to detect extremely low concentrations of airborn radioxenon, work automatically 24 hours a day without the need of continuous maintenance, and have a time resolution of no more than 24 hours.

The developed systems are: the Automatic Radioanalyzer for Isotopic Xenon (ARIX) [13], the Automated Radioxenon Sampler-Analyzer (ARSA) [14], the Swedish Automatic Unit for Noble Gas Acquisition (SAUNA) [15], and the Système de Prélèvement Automatique en Ligne avec l'Analyse du Xénon (SPALAX) [16].

ARIX is developed by Khoplin Radium Institute (KRI), Russia, ARSA by the Pacific Northwest National Laboratory (PNNL), USA, SAUNA by the Swedish Defence Research Agency (FOI), Sweden, and SPALAX by Commisariat à l'Énergie Atomique (CEA), France.

This work focuses on the SAUNA system, but the results may also be important for the ARSA and the ARIX systems which rely on similar radiation detection concepts, as will be discussed further in Section 3.2.

As a support for the radionuclide network, there are 16 radionuclide laboratories. These allow for reanalysis of suspicious samples, as well as routine controls of the performance of the stations.

The remainder of this thesis will focus on equipment used for radioxenon monitoring.

2.5 Civil uses of CTBTO data

The IMS network is unique of its kind and has a number of potential uses apart from the discovery of nuclear explosions. This was proven during, and after, the Tohuku earthquake and tsunami (also called the Great East Japan Earthquake), and the following accident in the Fukushima power plant in Japan in march 2011.

After the earthquake and tsunami that took many lives in the indian ocean region in december 2004, CTBTO was mandated to provide seismic and hydroacoustic data to tsunami warning centers. Today 13 countries, mainly in the Pacific and Indian ocean regions, have tsunami warning agreements with the CTBTO. These agreements allow them to obtain data from some IMS stations in near-real time, in order to improve their ability of issuing timely and precise tsunami warnings. Japan is one of these countries and they have stated that the CTBTO data helped them to issue fast tsunami warnings so that people in risk areas had time to reach higher ground [9].

The radioactivity released in the accident in the Fukushima power plant was first detected by the IMS station in Takasaki, 250 km from the power plant. The plume of radiation could then be followed as it dispersed, first to Russia, then the United States, followed by a spread over the entire northern hemisphere. Since the IMS is designed to detect very small concentrations of radioactivity it was possible to follow the cloud all the way, even though the levels were very low outside Japan.

The ATM also accurately predicted the spread of the radioactive plume. Member states had access to this data and could thus provide accurate information to the concerned public.

The Fukushima accident also lead to increased cooperation between CTBTO and other international organizations such as IAEA, the World Health Organization, and the World Meteorological Organization.

In addition to tsunami warnings and detection of radiation from nuclear accidents, the IMS data could also be used for a number of other things. Among these are detection of volcanic eruptions and a wide range of research on for example climate change, meteorology, and the worldwide background radiation [9].

3. Theory - Radioxenon detection and surface coatings

In this chapter theory relevant for the field of radioxenon detection is presented (Sections 3.1-3.4), as well as the memory effect (Section 3.5), which is the problem that we aim to solve with the work presented in this thesis. The approach of using surface coatings to remove this memory effect is also introduced (Section 3.6).

3.1 Why detect radioxenon?

In the event of a nuclear explosion a variety of fission products are created. In an underground explosion the majority of these will remain in the cavity formed by the explosion, and can thus not be detected by the IMS. However, around 15% of the fission products come in the form of noble gases, which due to their inert chemical properties can reach the surface and allow for detection. Even in the event of a well contained underground explosion, noble gases can travel through fractures and faults in the soil, and be pumped to the surface with the aid of barometric changes [17]. The detection of such gases can thus be crucial in order to identify an explosion as nuclear.

Xenon is created in large amounts in a nuclear explosion, since its mass is found close to the maximum of the fission mass yield curve for both uranium and plutonium [1]. Around 20 different isotopes of xenon are created in a nuclear explosion, of which four have half lives that are suitable for detection by the IMS. These are ^{131m}Xe ($t_{1/2}$=11.9 days), ^{133m}Xe ($t_{1/2}$=2.2 days), ^{133}Xe ($t_{1/2}$=5.2 days), and ^{135}Xe ($t_{1/2}$=9.1 h).

Half lives of the order of days are preferable since it is long enough for the isotopes to travel large distances in the air before decaying, so that they can reach an IMS measurement facility. It is also short enough so that xenon releases from for example nuclear power plants decay relatively fast, and the normal xenon background is kept at moderate levels [18].

3.1.1 Radioxenon decay

In this section the dominant decay modes of the four interesting radioxenon isotopes are described. The decays from ^{131m}Xe and ^{133m}Xe are described separately from ^{133}Xe and ^{135}Xe, and in Table 3.1 the most important emissions from each of the isotopes are summarized. A complete description of all possible decay modes can be found in Refs. [19] and [20].
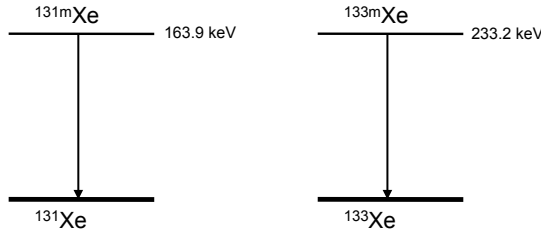
Figure 3.1. Decay schemes for ^{131m}Xe and ^{133m}Xe. The decay to the ground state takes place either through the emission of a gamma photon, or a conversion electron in combination with Xe X-rays (or Auger electrons).

^{131m}Xe and ^{133m}Xe

^{131m}Xe and ^{133m}Xe are isomers of ^{131}Xe and ^{133}Xe, respectively. An isomer is a long lived excited state of a nucleus, sometimes also called a metastable state [1]. The isomer decays to the ground state nucleus through isomeric transition, where a gamma ray carrying the excitation energy is emitted.

Competing with the emission of a gamma ray is internal conversion, where a conversion electron (CE) is emitted, as described in Section 1.2.1. The emission of the CE creates a vacancy in the shell where it used to be bound. This vacancy is almost instantaneously filled with an electron from an outer shell, resulting in the emission of characteristic X-rays carrying the difference in binding energy between the different shells[1].

Figure 3.1 shows the decay schemes of the two radioxenon isomers suitable for detection in IMS. The transition indicated by the arrow can, as explained, either take place through the emission of a gamma ray carrying the full excitation energy, or internal conversion. For both ^{131m}Xe and ^{133m}Xe the decay to the ground state is dominated by internal conversion. The dominating CE's are the ones originating from the K-shell, resulting conversion electrons with energies of 129 keV from ^{131m}Xe, and 199 keV from ^{133m}Xe. The K-shell CE's are in most cases emitted together with a Xe X-ray of around 30 keV.

The energies and total intensity for CE's from higher shells can be found in Table 3.1. These higher energy CE's are emitted together with X-rays (or Auger electrons) of lower energies, compared to the X-rays emitted together with the K-shell CE's.

The ground state of ^{131}Xe is stable, but the one of ^{133}Xe is not, and its decay is described in the following paragraph.

^{133}Xe and ^{135}Xe

Both ^{133}Xe and ^{135}Xe decay through β^- emission, which is described in Section 1.2.1.

---

[1]An alternative to X-ray emission, is the emission of so called Auger electrons which carries the excess energy.

Figure 3.2(a) shows the decay scheme of ^{133}Xe. The daughter nucleus of ^{133}Xe is ^{133}Cs, which is stable. There are various possible beta decays, but the dominating one has an endpoint energy of 346.4 keV, taking place in 98.5% of the decays (indicated by ①︎ in the figure). This dominating decay leaves the nucleus at a 80.99 keV excited state of ^{133}Cs. The transition ②︎ to the ground state of ^{133}Cs takes place either by emission of an 80.99 keV gamma ray, or internal conversion with the emission of a CE in association with Cs X-rays (or Auger electrons). The dominating CE is from the K-shell and has an energy of 45 keV, and the corresponding K X-ray has an average energy of 31.6 keV.

The branching ratio of the 80.99 keV gamma ray is 36.9%, and the branching ratio of the 45 keV K-shell CE together with an X-ray of around 30 keV is 47.2%.

^{135}Xe has ^{135}Cs as daughter nucleus, and its decay scheme is shown in Figure 3.2(b). The decay is dominated by a β^- decay with an endpoint energy of 915 keV ③︎, leaving the daughter nucleus at a 249.8 keV excited state.

The transition ④︎ to the ground state takes place either through emission of a 249.8 keV gamma ray, or internal conversion. For this isotope it is the gamma emission that is dominating, having a branching ratio of 90%. The daughter nucleus, ^{135}Cs, is in this case also radioactive, but with a very long half life of 2.3×10^6 years.

In Table 3.1 the energies and intensities of the dominating transitions (corresponding to the bold arrows in Figure 3.2) are shown.

3.2 Radioxenon detection

As mentioned in Section 2.4 there are 4 different radioxenon detection systems developed for use in the IMS: ARIX, ARSA, SAUNA, and SPALAX.

All systems sample air during 12-24 hours and extract a xenon sample from this air. The xenon is extracted from the air by passing it through activated charcoal which adsorbs xenon more easily than most other atmospheric gases. The adsorbed xenon is released in a second step by heating and with the aid of an inert carrier gas such as helium or nitrogen. The sample is further purified by a series of gas chromatographic steps. The final sample containing xenon (both stable and active) and sometimes small remnants of radon are passed into the detector part of the respective system with the aid of a carrier gas [21].

For the activity measurement, three of the systems make use of the fact that all four radioxenon isotopes emit coincident fast electrons and photons within a reasonably small energy range. The activities in these systems are measured by beta-gamma coincidence spectroscopy, which is described in detail in Section 3.2.1, and more specifically for the SAUNA system in Section 3.2.2.
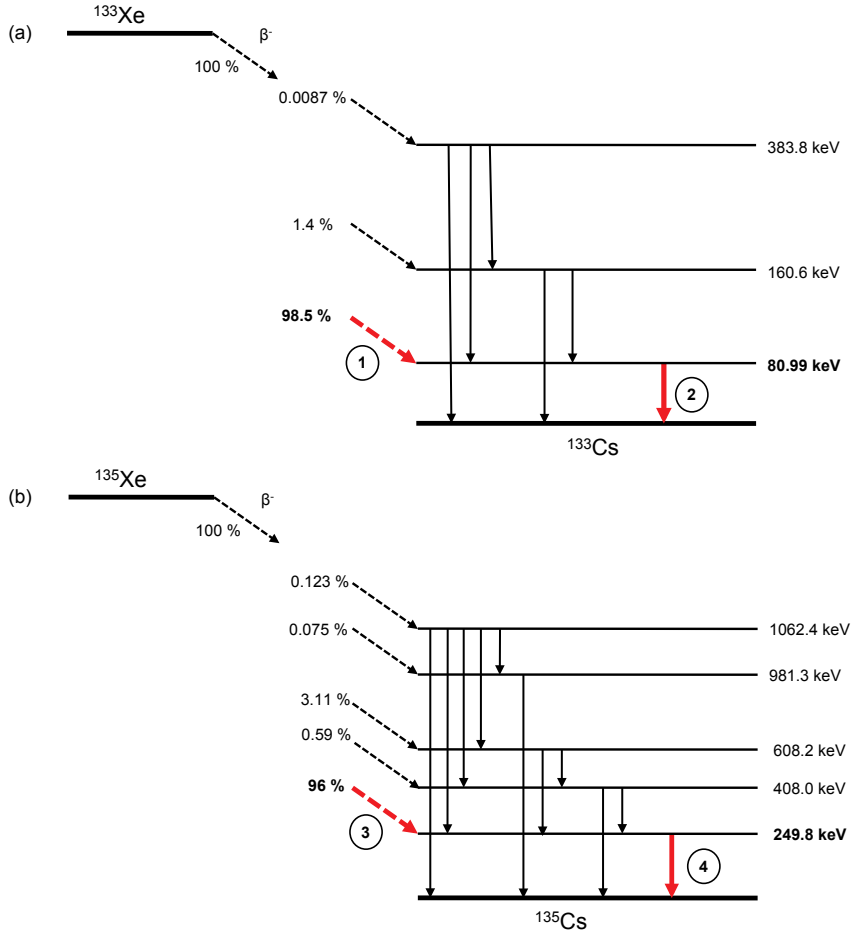
Figure 3.2. Decay scheme for ^{133}Xe (a), and ^{135}Xe (b). The dashed arrows correspond to β^- decay, and the solid ones are gamma transitions which in some cases can be substituted by internal conversion. The numbered transitions correspond to the strongest transitions for each of the isotopes, and are described further in the text.

Table 3.1. *The dominant emissions from the radioxenon isotopes of interest for detection by the IMS [19]. The intensity (or branching ratio) equals the fraction of all decays that result in the emission the respective type of radiation. The X-ray energies are given as the intensity weighted average over all K X-rays. X-rays other than the K X-rays are omitted from the table due to their low energy, as are the Auger electrons due to their low intensity. The radiations in bold correspond to those analyzed in the beta-gamma coincidence spectrum described in Section 3.2.1*

Isotope	Half life	Radiation	Energy (keV)	Intensity (%)
^{131m}Xe	11.930 d			
		gamma	163.9	1.95
		CE (K)	**129.4**	61.6
		CE (Higher shells)	158.8-163.9	36.5
		K X-ray	**30.4** (Average)	54.7
^{133m}Xe	2.198 d			
		gamma	233.2	10.12
		CE (K)	**198.7**	62.9
		CE (Higher shells)	227.8-233.2	26.8
		K X-ray	**30.4** (Average)	55.9
^{133}Xe	5.2474 d			
		beta	**346.4** (Endpoint)	98.5
		gamma	**80.99**	36.9
		CE (K)	**45.01**	52.8
		CE (Higher shells)	75.3-80.98	10.0
		K X-ray	**31.6** (Average)	47.2
^{135}Xe	9.14 h			
		beta	**915** (Endpoint)	96.0
		gamma	**249.79**	90.0
		CE (K)	213.8	5.61
		CE (Higher shells)	244.0-249.8	1.03
		K X-ray (Average)	31.6	4.95

The fourth system, SPALAX, uses a high purity germanium detector (HPGe) for the activity measurement. A HPGe detector is a semiconductor detector, widely used in gamma ray spectroscopy due to its high resolution [2]. SPALAX measures the dominant gamma rays from the decay of each of the four radioxenon isotopes (see Table 3.1). Since the dominant gamma lines from the two metastable isotopes have relatively low intensities, the X-rays from these isotopes are also analyzed in order to increase the sensitivity. The measurement of the X-rays alone would not be enough to determine the activities of both isotopes, since they have the same energies. The X-ray analysis must therefore be combined also with the measurement of the gamma rays [21].

3.2.1 Beta-Gamma coincidence spectroscopy

The overlapping spectra in both the photon and electron domain, and the low intensity gamma lines from the metastable isotopes, makes the use of beta-gamma coincidence spectroscopy a convenient choice for measuring the activity of each isotope [14, 22, 15].

This approach is adopted by the SAUNA, ARIX and ARSA systems.

When it comes to internal conversion, the X-rays are emitted very rapidly after the CE. Furthermore, the lifetimes of the excited states of ^{133}Cs and ^{135}Cs are of the order of nanoseconds. The result is that the beta decay, and the following gamma or CE + X-ray are emitted almost instantaneously.

A beta-gamma coincidence spectrometer generally incorporates multiple detectors, where electrons are detected in one detector, and photons in the other. An event is recorded if an interaction has been detected in both detectors within a short time interval defined by a coincidence window. The coincidence window states the time interval within which two events are considered to originate from the same decay.

The result of the measurement is a two-dimensional (2D) spectrum where each event is characterized by both a photon energy and an electron energy. An added advantage of the coincidence technique is that the influence of ambient background activity is drastically reduced, since all events without a coincident complementary radiation are removed from the spectrum.

Figure 3.3 shows a schematic picture of a 2D coincidence spectrum containing all four xenon isotopes. On the x-axis is the beta (or CE) energy of the event, and on the y-axis is the gamma (or X-ray) energy. The different regions in the figure correspond to the dominating decays of each isotope:

^{131m}**Xe (green):** A 129 keV CE in coincidence with a Xe X-ray of around 30 keV.

^{133m}**Xe (blue):** A 199 keV CE in coincidence with a Xe X-ray of around 30 keV.

^{133}**Xe (yellow):** The decay from this isotope is seen in two different regions, both originating from a beta decay with endpoint energy of 346 keV. The beta decay can either be followed by a 81 keV gamma emission, or a 45 keV CE together with a 30 keV X-ray, as explained in Section 3.1.1. The upper region shows the beta distribution in coincidence with the 81 keV gamma ray, and the lower region shows the same beta distribution in coincidence with the CE and a 30 keV X-ray. The lower region is shifted in beta energy since the 45 keV from the CE is added to the beta energy in each event.

^{135}**Xe (red):** The dominating beta decay with endpoint energy of 910 keV is detected in coincidence with a 250 keV gamma ray.
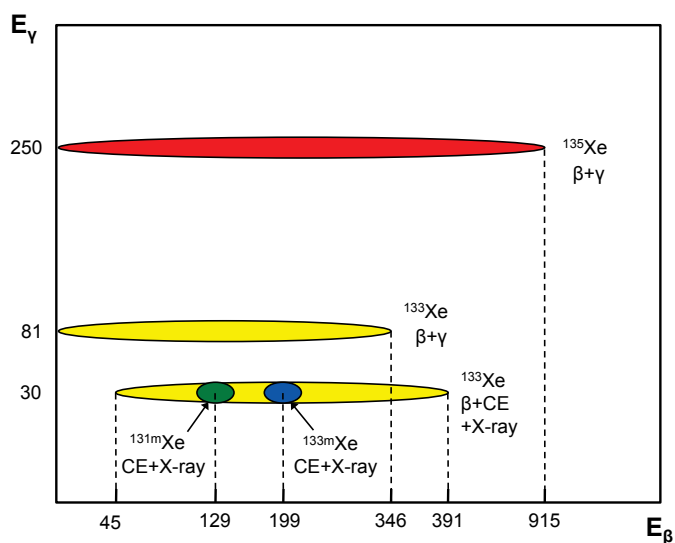

Figure 3.3. Schematic picture of a 2D beta-gamma coincidence spectrum containing ^{135}Xe (red), ^{133}Xe (yellow), ^{131m}Xe (green), and ^{133m}Xe (blue). All energies are given in keV. The x-axis corresponds to the electron (beta or CE) energy and the y-axis corresponds to the photon (gamma or X-ray) energy. A real spectrum containing ^{133}Xe is shown in Figure 5.2 in Chapter 5.

Determination of atmospheric concentrations

From a measured 2D-spectrum, with the characteristics of the one shown in Figure 3.3, the activities of each of the xenon isotopes in the measured sample can be determined, and from these their respective atmospheric concentrations. For the SAUNA system, the analysis of the spectra is based on the so called Net Count Calculation method [23, 24]. This method is based on 10 regions of interest (ROIs), defining interesting parts of the spectrum, as shown in Figure 3.4.
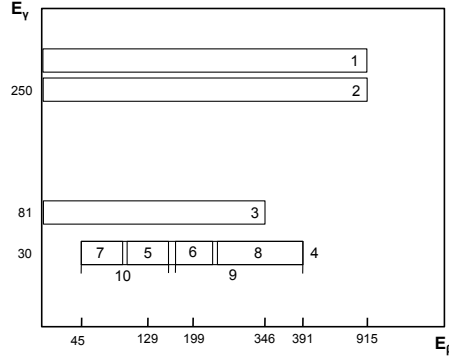
Figure 3.4. Regions of interest used in the analysis of radioxenon beta-gamma spectra.

Sometimes the sample can contain radon contamination, which contributes to the background in the measured spectrum, through the decay of its daughters ^{214}Bi and ^{214}Pb. ROI 1 contains counts from ^{214}Pb, and is used to correct for the radon contamination. The other ROIs can be compared to Figure 3.3, and are used to determine the activity of each of the four xenon isotopes. ROI 2 contains counts from ^{135}Xe, and ROI 3 counts from ^{133}Xe. ROI 4 contains counts from both ^{133}Xe, ^{131m}Xe, and ^{133m}Xe, and therefore ROI 5-10 are used to determine the number of counts related to each of these three isotopes.

For each isotope i the net number of counts c_i corresponding to a certain decay can be determined by correcting for interferences from other isotopes as well as background.

From the net number of counts, the atmospheric concentration C_i [Bq/m^3] of each of the isotopes at the time of the start of the sample collection, can be determined according to [23]:

$$C_i = \frac{c_i}{\varepsilon_{\beta\gamma}\beta\gamma} \frac{\lambda^2}{F_C F_P F_A} \frac{t_{coll}}{V}, \tag{3.1}$$

where the different parameters correspond to:

c_i = The net number of counts from a certain decay of isotope i.

$\varepsilon_{\beta\gamma}$ = The absolute detection efficiency in the ROI containing the decay of interest.

$\beta\gamma$ = The branching ratio of the decay.

λ = The decay constant of isotope i.

$F_C = 1 - e^{-\lambda t_{coll}}$, is a factor correcting for decay of the sample activity during the collection time t_{coll} of the air volume.

$F_P = e^{-\lambda t_{proc}}$, is a factor correcting for decay of the sample activity during the processing time t_{proc} of the xenon sample.

$F_A = 1 - e^{-\lambda t_{meas}}$, is obtained by integrating the number of decays occurring during the measurement time, t_{meas}, of the sample.

t_{coll} = The collection time of the air sample.

V = The sampled air volume. V is found by dividing the volume of the xenon sample with the known concentration of stable xenon in air. The volume of the xenon sample is determined in the gas chromatograph in the processing unit of the system, and the radioactive xenon only constitute a very small fraction of the total xenon sample.

The main contributions to the uncertainty in a calculated concentration, are the uncertainties in the net number of counts c, and in the air volume V [15].

3.2.2 The SAUNA system

Almost half of the radioxenon detection systems used in the IMS are SAUNA systems. The prototype SAUNA was developed by the Swedish Defence Research Agency (FOI) [15]. The system was commercialized in 2004, and the current version, SAUNA II, is manufactured by the company Scienta SAUNA Systems [25].

The system consists of three main parts, performing sampling, processing and activity measurement of a xenon sample. In the sampling and processing units a xenon sample of typically 1.3 cm^3 is extracted from around 15 m^3 of air. The xenon sample is then introduced into a detector where the activities of ^{131m}Xe, ^{133m}Xe, ^{133}Xe, and ^{135}Xe are measured during 11 hours.

The detector is a beta-gamma coincidence spectrometer consisting of a 6.2 cm^3 cylindrical plastic scintillator cell, inserted into a drilled hole in a NaI(Tl) crystal, as illustrated in Figure 3.5. The plastic scintillator cell also acts as a container for the xenon sample during the measurement.

Electrons are less penetrating than photons, so the beta particles and conversion electrons are detected in the plastic scintillator cell, and the gammas and X-rays are detected in the NaI(Tl) crystal. The thickness of the walls of the plastic scintillator cell is 1 mm, chosen so that the 346 keV electrons from the β^- decay of ^{133}Xe are fully stopped.

The NaI(Tl) crystal is coupled to one PM-tube, and the plastic scintillator cell has one PM-tube attached at each end. An event is recorded in the 2D histogram if a signal is measured in all three PM-tubes in coincidence. The detector design is based on the one used in the ARSA system [14].

The system contains 2 identical detector units working in parallel where one detector measures a sample while the other one measures a gas background in the empty detector after the previous measurement. The gas background measurement is needed to correct for any residual activity left in the detector from previous samples. This residual activity is referred to as the memory effect, which is described further in Section 3.5.
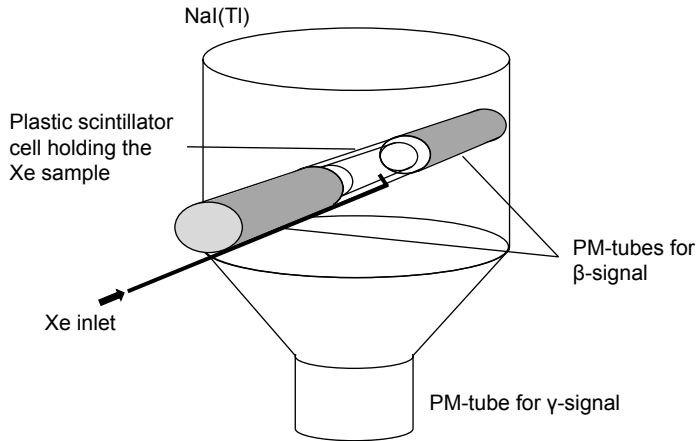
Figure 3.5. The SAUNA detector. The xenon sample is located inside the plastic scintillator cell during the measurement. The signal from the NaI(Tl) crystal is read out by one PM-tube, and the signal from the plastic scintillator by two PM-tubes.

3.3 Radioxenon sources

Nuclear explosions are not the only source of radioxenon in the atmosphere, a fact that makes the task of identifying an event as nuclear rather complicated. The detection of presence of radioxenon in the atmosphere is thus not enough to conclude that a nuclear explosion has taken place. The absolute activities of the different isotopes are not enough either, since the gases are often very diluted before reaching an IMS station. This has lead to the use of isotopic ratios to distinguish an explosion from civilian sources [26].

The main contributors to the global radioxenon background are nuclear power plants (NPPs), and medical isotope production facilities (MIPFs) [27, 28]. Common for NPPs, MIPFs, and nuclear explosions is that in all cases xenon is produced as by-product in neutron-induced fission. The main difference between the three cases is the neutron irradiation time. In uranium or plutonium nuclear bombs this irradiation is almost instantaneous. The most common reaction in MIPFs is neutron irradiation of a high enriched uranium (HEU) target with the aim to produce ^{99}Mo/^{99m}Tc. In this case the irradiation time is on the order of days. The longest irradiation times are found in NPPs where the irradiation time of the nuclear fuel is of the order of months or years. The different irradiation times is something that has been found to have great impact on the ratios between the different xenon isotopes [27, 28].

Even though the isotopic ratios may help in distinguishing between nuclear explosions and other sources, it is quite likely that not all four isotopes are detected by the IMS, making it very important to have a good knowledge of

the radioxenon background and potential sources in the vicinity of each measurement station.

3.3.1 Nuclear explosions

In a nuclear explosion, radioxenon can be produced both as a direct fission product, or through decay from parent nuclei also created in the explosion [18]. Because of this, one usually speaks about two different fission yields of a certain isotope; the independent yield and the cumulative yield.

The independent yield of an isotope is the fraction of all fissions resulting in the direct formation of that isotope.

The cumulative yield takes into account also the decay chains of other fission products. The ingrowth from decay of all parent nuclei (also created in the fission event), that eventually decay to xenon thus adds to the yield.

Table 3.2 lists the expected yields from all four isotopes in the case of thermal fission of ^{235}U. Listed are also the expected isotopic ratios in the two cases which, as can be seen, differ by several orders of magnitude for both listed ratios.

Table 3.2. *Xenon yields and isotopic ratios from thermal fission of ^{235}U [28].*

	Independent yield (%)	Cumulative yield (%)
^{131m}Xe	3.48E-07	4.05E-02
^{133m}Xe	1.89E-03	1.89E-01
^{133}Xe	6.66E-04	6.70E+00
^{135}Xe	7.85E-02	6.54E+00
^{133m}Xe/^{131m}Xe	5.43E+03	4.67E+00
^{135}Xe/^{133}Xe	1.18E+02	9.76E-01

The ratios expected to be measured by an IMS station will thus depend on when the noble gases were separated from their parents

If the noble gases are separated from the rest of the fission products at the time of the explosion, it is only the independent yield that will be observed. If, on the other hand, the noble gases are contained together with their parents four hours or days before being vented, the ingrowth from the parent nuclei will be significant, which will affect the isotopic ratios that are measured.

Furthermore, the different half lives of the four isotopes cause the isotopic ratios to change in time. The ratios thus depend on when they are measured relative to the explosion, and the time of separation between gases and other fission products.

There are thus a range of isotopic ratios, all consistent with a nuclear explosion, which is important to take into account when differentiating nuclear explosions from civilian sources. By studying the isotopic ratios one may also obtain information about the timing of the event.

3.3.2 Nuclear power plants

For NPPs the radioxenon isotopic ratios reach equilibrium values after a couple of weeks of full power operation. During reactor shutdown and startup these ratios can however change quite drastically, and it is thus not enough to only consider the equilibrium value for source discrimination [27].

In Ref. [27] simulations of both the expected ratios from light water reactors, and explosion ratios were performed, resulting in an approach that can be used to differentiate between NPPs and a nuclear explosion. This approach is illustrated in Figure 3.6. Two isotopic ratios have been plotted against each other in a log-log plot, where the isotope with the longer half life is in the denominator on each axis. The red dashed line separates the ratios in a reactor domain to the left of the line, and an explosion domain to the right. The slope of the separation line is determined by the decay constants of the four isotopes, so that the explosion ratios always end up in the explosion domain, independent of when they are measured. Theoretically, all radioxenon created in the fuel matrix in a nuclear reactor should end up to the left of the line, except during the first 20-30 days of irradiation of fresh fuel. The expected ratios during these first days unfortunately overlap with the ones expected from a nuclear explosion.
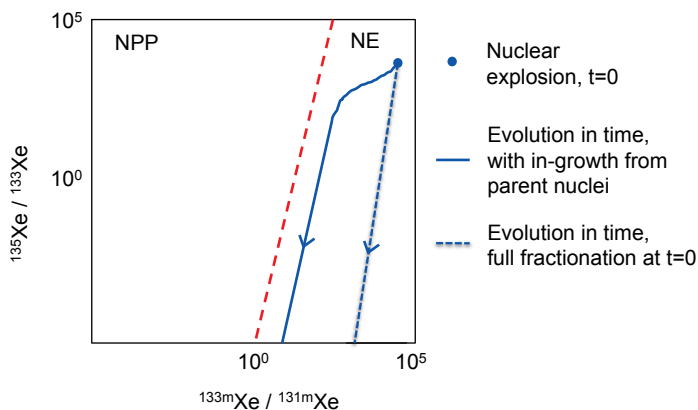

Figure 3.6. Schematic picture illustrating the source discrimination approach proposed by Kalinowski et. al., involving multiple isotopic ratios [27]. The red dashed discrimination line divides the plot in a nuclear power plant domain (left), and a nuclear explosion domain (right). The blue dot represent the time of the explosion, and the lines the evolution in time of the expected ratios. The solid line is when in-growth from parent nuclides takes place, and the dashed one when the radioxenon gas is separated from the other fission products at the time of the explosion.

The blue line in the figure represents the ratios from a nuclear explosion, where the dashed line shows the behavior over time after full fractionation at the time of the explosion, and the solid line takes into account ingrowth from

parent nuclei. The dot represents the time of the explosion, and both ratios decrease with time since the longer lived isotope is in the denominator in both cases.

In this figure all four isotopes are used, but if not all isotopes are detected, it is also possible to do similar graphs with less than four isotopes. However, such graphs do not provide as efficient screening as if all four isotopes are measured. This screening approach has been validated with measured radioxenon concentrations, as well as reported annual releases from NPPs [29].

3.3.3 Medical isotope production facilities

Medical isotope production facilities have proven to be the major source of radioxenon in the atmosphere, even though there are much fewer MIPFs than NPPs [28]. One problem with MIPFs is that the irradiation times of the HEU target is only of the order of days, resulting in isotopic ratios very similar to the ones expected from a nuclear explosion. It is thus not possible to discriminate between these two sources by using a simple discrimination line. The ratios expected in a release from a MIPF are affected mostly by the irradiation times.

Suggestions to solve this issue are that the MIPFs prolong their irradiation times and implement processes that reduce the xenon emissions. It would also be very useful to use measurements of the emissions of xenon in the stack, together with atmospheric transport modeling in the analysis of IMS data.

3.4 Events in the past

Since the start of the construction of the IMS, the Democratic People's Republic of Korea (DPRK) have announced 3 nuclear test explosions, in 2006, 2009 and 2013.

2006

On October 9 in 2006, DPRK announced that they had performed a nuclear test, and the event was also detected by the seismic network in the IMS. At that time the closest noble gas systems in operation were located in Ulaanbaatar (Mongolia), Spitsbergen (Norway), Stockholm (Sweden), and Yellowknife (Canada). Due to the winds at the time the only place where radioxenon from the explosion possibly was detected was in Yellowknife, 7000 km away from the explosion site [30]. ^{133}Xe was seen in elevated concentrations around 2 weeks after the explosion, but none of the other isotopes. The elevated activity concentration could however not be explained by any other source in the vicinity of the noble gas system. Atmospheric transport modeling also showed the xenon signal to be consistent with a release from the explosion site in DPRK at the time of the event.

However, a non-IMS detection provided more conclusive evidence. A mobile SAUNA xenon sampler, [25], was sent to South Korea days after the explosion, and used to collect to xenon samples close to the DPRK border. The samples were then transported to FOI in Sweden for analysis [31]. The measurements showed measurable concentrations of both ^{133}Xe and ^{133m}Xe consistent with a nuclear explosion.

The above mentioned measurements all contained xenon concentrations of the order of mBq/m^3, a fact stressing the importance of very low detection limits of the IMS noble gas systems. The importance of knowledge of the radioxenon background, as well as potential radioxenon sources, in combination with atmospheric transport modeling were also proven to be crucial in order to identify the explosion as nuclear.

2009

In May 2009 DPRK announced their second test explosion. Also this test was picked up by the seismic network in the IMS, and its location was found to be close to the 2006 test. This test was found to be around 4 times more powerful than the first one. However, no radioxenon was measured after the explosion, even though the density of measurement facilities in the area was higher than 2006. [9, 32].

2013

The final announced test by DPRK took place on February 12, 2013. Again the event was detected and localized by the seismic network. The location was close to the previous sites, and the magnitude of the explosion around 10 times higher than in 2006 [32]. No release of radioactivity was measured in the days or weeks following the explosion. However, in april 2013, around 8 weeks after the event, elevated atmospheric concentrations of ^{131m}Xe and ^{133}Xe were measured in Takasaki, Japan as well as in Ussuryisk, Russia. At both locations the isotopic ratios and atmospheric modeling showed that the explosion site was a likely source of the release. The proposed scenario is that the explosion tunnel was entered at this time, in order to investigate the explosion, and that this caused a release of radioxenon. The measurements prove that the IMS is capable of detecting radioxenon releases from a nuclear explosion at multiple locations, even a long time after the event took place [32].

3.5 The memory effect

One problem with the current design of the SAUNA system is that part of the xenon sample diffuses into the plastic scintillator material of the beta cell during the measurements [33]. This is also a problem for the ARSA and the ARIX systems, which also contain beta gamma coincidence spectrometers involving plastic scintillators [21, 34].

Today this memory effect is accounted for by doing a gas background measurement of the evacuated cell, prior to each sample measurement. The residual activity in the gas background can then be subtracted from the sample activity. For this reason, the SAUNA system contains two detectors working in parallel to allow for continuous monitoring. This approach is however not ideal, and leads to an elevation of the system detection limit. The gas background measurement contains counts from both memory effect and ambient background. The influence of these two contributions, and how the background correction is performed, is illustrated in Figure 7 in Paper III.

Figure 3.7 shows the count rate of ^{133}Xe in the ROI at 81 keV gamma energy and 0-346 keV beta energy (ROI 3 in Figure 3.4), in a series of sample measurements, and gas background measurements. The data is taken from an IMS SAUNA system installed in Charlottesville, VA, USA. The shown count rate is the net count rate, where background counts and interferences from other isotopes have been subtracted from the total measured number of counts in the ROI. It is from this figure clearly seen that a high count rate in a sample measurement is followed by an elevated count rate also in the following gas background measurement. It is also seen that a strong sample leaves traces of residual activity in several subsequent gas background measurements.
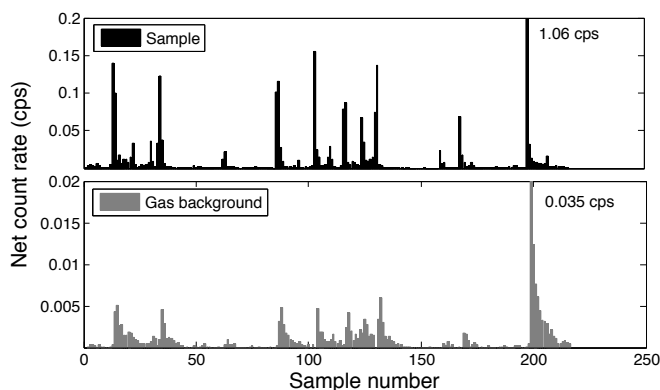

Figure 3.7. The memory effect illustrated through a series of sample (top), and gas background measurements (bottom). Note that the scales on the y-axes are different.

In Figure 3.8, part of the data in Figure 3.7 has been used to plot the ^{133}Xe count rate in the gas background measurements as a function of the count rate in the previous sample measurement. Only the data where the sample count rate is above 0.035 cps has been used, in order to investigate how much of the sample activity is left in the cell in the subsequent gas background. The gas background measurements with residual activity from sample measurements further back in time, like those seen after the strong sample around sample

number 200 in Figure 3.7, are thus not included. The discrimination value was chosen by visually inspecting the data set shown in Figure 3.7.

The data has been fitted with a linear function, with a resulting slope of 0.032. A rough estimate of the memory effect, defined as fraction of the sample activity left in the cell in the following gas background measurement, is thus 3-4%.
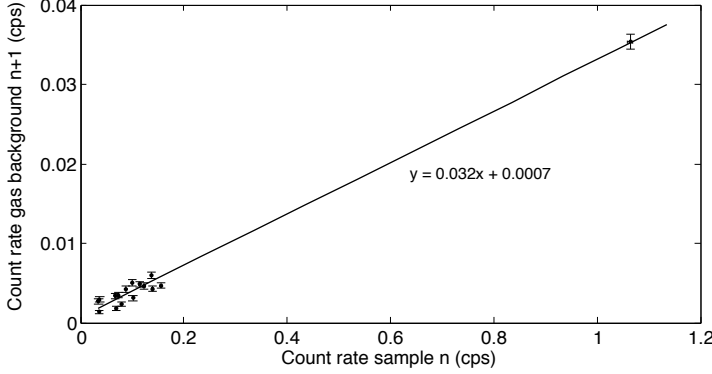

Figure 3.8. ^{133}Xe count rate in a series of gas background measurements, as a function of the count rate in the previous sample measurement.

As previously mentioned, the ultimate result of the memory effect is that it elevates the detection limit of the system, even if it is compensated for by subtraction of the gas background counts [35].

When it comes to the limits of detectability, there are two quantities that are of interest, the critical limit L_c, and the minimum detectable concentration, MDC.

Critical limit L_c

The critical limit L_c is used to decide if activity is present in the measured sample or not. It is determined by the statistical fluctuations in the number of background counts in a given ROI. The net number of counts in an ROI is the total number of counts minus the background counts. If the net number of counts exceeds the L_c, it is assumed that some real activity is present in the sample [36, 4]. It is common to define L_c as the critical limit ensuring a false positive rate[2] of no more than 5%, given by:

$$L_c = 1.645\sqrt{2}\sigma_{bg} = 2.326\sigma_{bg}, \tag{3.2}$$

---

[2]A false positive in this context is that it is concluded that it exists a certain xenon isotope in the atmosphere, when it in fact does not. It is not referred to a conclusion regarding wether a nuclear explosion has taken place, since there are other radioxenon sources.

where σ_{bg} is the standard deviation associated with the number of background counts. This yields a standard deviation of $\sqrt{2}\sigma_{bg}$ for the net number of counts since the standard deviation of the measurement equals the standard deviation of the background, when no activity is present. The factor 1.645 comes from the fact that for a Gaussian distribution 5% of all observations falls above 1.654σ over the mean of the distribution.

In this particular application it is common to express the limit L_c as an activity concentration. This expression is obtained by setting c_i in Eq. 3.1 equal to $2.326\sigma_{bg}$:

$$L_c = \frac{2.326\sigma_{bg}}{\varepsilon_{\beta\gamma}\beta\gamma} \frac{\lambda^2}{F_C F_P F_A} \frac{t_{coll}}{V} \tag{3.3}$$

If an activity concentration above L_c is inferred from the measurement, it is concluded that there is some real activity in the sample. By defining L_c as above, there is a 5% chance for a false positive.

Minimum Detectable Concentration, MDC

The MDC is the **real** activity concentration needed to ensure a reasonably low false negative rate, given the critical limit L_c. Due to the statistical fluctuations always present in any counting system, the observed number of counts from a given source will vary around the true mean number of counts. The minimum value for the mean net number of counts c_{min}, that ensures a false negative rate of less than 5%, when L_c is defined according to Eq. 3.2, can be expressed as [36]:

$$c_{min} = 4.65\sigma_{bg} + 2.71 \tag{3.4}$$

The MDC is defined as an atmospheric concentration and calculated by substituting the net number of counts c in Eq 3.1 for c_{min} [23]:

$$MDC = \frac{4.65\sigma_{bg} + 2.71}{\varepsilon_{\beta\gamma}\beta\gamma} \frac{\lambda^2}{F_C F_P F_A} \frac{t_{coll}}{V} \tag{3.5}$$

A full derivation of Eq. 3.2 and 3.4, which are both standard equations, can be found in Refs. [4] and [36].

Figure 3.9 shows L_c of ^{133}Xe, as a function of the atmospheric ^{133}Xe concentration (C) in the previous sample measurement. Here the L_c is expressed as an atmospheric concentration, according to Eq. 3.3.

In Figure 3.8 it was shown that in the case of only short term memory effect, the gas background depends linearly on the activity measured in the previous sample. If counting statistics is the only source of fluctuations in the background, σ_{bg} is given by the square root of the number of background counts. Since the background depends linearly on the sample activity concentration, it is reasonable to express L_c as a function of $\sqrt{C}$, where C is the concentration in the previous sample.
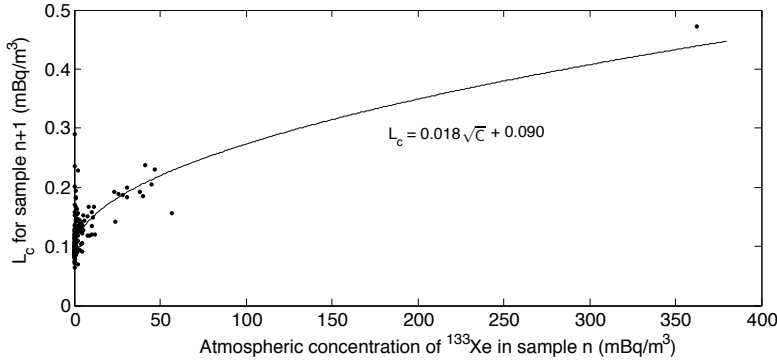
Figure 3.9. The critical limit for detection L_c as a function of the atmospheric activity concentration (C) of the previous sample. The line corresponds to a linear fit of L_c as a function of $\sqrt{C}$ for all samples with a concentration above 2 mBq/m^3.

In Figure 3.9 the L_c data has been fitted with a first order polynomial, where $\sqrt{C}$ is the variable. The constant is included to account for the constant detector background not affected by C. Only the data where the activity concentration in the sample is above 2 mBq/m^3 is included in the fit, in order to remove data points where L_c is elevated due to long term memory effect from samples measured further back in time. These points are seen in the figure as high L_c values for very low concentrations. The discrimination limit was chosen through ocular inspection of the data set.

In the case of this SAUNA system located in Charlottesville, a typical sample contains a few mBq/m^3 of ^{133}Xe, which results in a critical limit between 0.1 and 0.2 mBq/m^3. As seen in Figure 3.9, a high sample activity of around 300 mBq/m^3 increases this limit by almost a factor of 4.

The radioxenon detection systems used in the IMS are required to have an MDC of less or equal than 1 mBq/m^3, for ^{133}Xe [21].

From Eqs. 3.3 and 3.5 it is seen that the MDC $> 2L_c$, and the high concentration in this data set thus results in an MDC very close to the required limit.

In order to assure a high reliability of the system it would thus be a great improvement if the memory effect could be removed since it directly elevates the detection limits. A lower detection limit would also result in lower uncertainties for the measured radioxenon concentrations, which could be important in order to identify the source of the radioactive gas, as described in Section 3.3.

In an ideal system with no memory effect, the gas background measurements would be obsolete. A memory effect reduction could thus allow for removal or reduction of the gas background measurements, leading to longer sample measurement times.

An additional motivation for memory effect reduction are the systems currently under development for use in On Site Inspections. Such systems are based on subsoil sampling close to a suspected nuclear explosion site. The amounts of radioactive xenon would thus be much higher than what is observed in the IMS systems, and the memory effect would therefore also be a bigger problem.

Finally, a system without memory effect would allow for recalibration or quality controls of the systems using radioactive gases. With the memory effect, such experiment would result in residual activity left in the detector for months.

3.5.1 Potential solutions

There are various potential approaches for achieving a memory effect reduction. In Ref. [37] the plastic scintillator cell was exchanged for an inorganic cerium doped scintillator made of yttrium aluminum perovskite (YAP). This YAP cell presented a very small memory effect. However, with the detector geometry used, the X-rays at around 30 keV were absorbed in the YAP detector material due to its high effective atomic number. The X-rays could thus not be detected in the surrounding NaI(Tl) crystal, and a much thinner YAP cell would be needed for the technique to work.

Inorganic scintillating glass is another alternative material that has been discussed, but also this detector would need to be very thin in order to let the X-rays through.

Another potential solution that has been discussed, is to saturate the plastic detector with stable xenon, so that there is no room for the radioactive atoms. This approach is investigated in Chapter 4 in this thesis, and was found not to work.

The approach focused on in this thesis, is to coat the existing plastic scintillator cell with a material working as a gas diffusion barrier. An advantage with this solution is that it requires minimal changes of the existing system. The only thing that needs to be exchanged is the plastic scintillator cell. Provided that a barrier is achieved without impairing detector resolution and efficiency, the analysis of the measurement data does no need to be altered either.

3.6 Surface Coatings as diffusion barriers

The approach selected in this thesis is to coat the surfaces of the plastic scintillator exposed to the radioxenon sample with a material that is able to stop the xenon diffusion. This has previously been tested with pure metals that were deposited onto a plastic scintillator using electron beam lithography [37]. The problem with these coatings were that some of them easily flaked off, and that

the light collection in the detector was impaired, and hence also the energy resolution.

For the work presented in this thesis the choice of coating materials was based on a number of desirable characteristics:

- The coating should be a good gas diffusion barrier.
- It should be transparent to the scintillator light, so that part of the signal is not lost in the coating. This requirement is fulfilled by materials having a band gap above 3.2 eV, which is the energy of the 380 nm photons at the high energy end of the emission spectrum of BC-404 [38].
- The refractive index of the coating should be close to 1.58, which is the refractive index of the plastic scintillator material, to minimize the risk of disturbing the light collection in the detector.
- The technique used to deposit the coating material should work at a relatively low temperature, since the softening point of the plastic scintillator material is as low as 70°C [38].
- The coating technique needs to be able to coat the inside of a cylinder with a uniform film. This requirement eliminates all coating techniques that requires line of sight.

Two transparent coatings were chosen for further investigation, Al_2O_3 deposited using Atomic Layer Deposition (ALD), and SiO_2 deposited with Plasma Enhanced Chemical Vapor Deposition (PECVD). Both these coatings are used as gas diffusion barriers in a variety of applications. The materials have also previously been deposited onto polymers in for example food packaging and organic light emitting devices [39, 40]. Experiments with these materials are summarized in Chapter 5, and described in detail in Papers I and III.

A theoretical study of graphene as a diffusion barrier for this application is described in Section 5.4, and Paper IV.

3.6.1 Atomic Layer Deposition

Atomic Layer Deposition (ALD) is a technique that is widely used to deposit thin films [41]. In this process the substrate to be coated is sequentially exposed to the reactant gases, which are called precursors.

The reactions between the surface of the substrate and the precursors are self-terminating, in the sense that only one atomic layer is deposited in each exposure, regardless of its duration (given that sufficient time is allowed for the surface to be covered with one layer). In Figure 3.10 the ALD process is illustrated in 4 steps.

Step 1: In the first step the substrate is exposed to the first precursor gas. The gas molecules reacts with the surface of the substrate an atomic layer is formed.

Step 2: After the exposure of the first reactant the ALD reactor is flushed with an inert gas in order to remove excess precursor molecules, as well as by-products from the reaction. Since the substrate-precursor reaction is self-terminating, the substrate is left covered with one monolayer of molecules.

Step 3: The substrate is exposed to the second precursor gas which reacts with the surface.

Step 4: The excess precursor gas and reaction by-products are again removed from the ALD reactor. The result is a monolayer of the desired coating material.
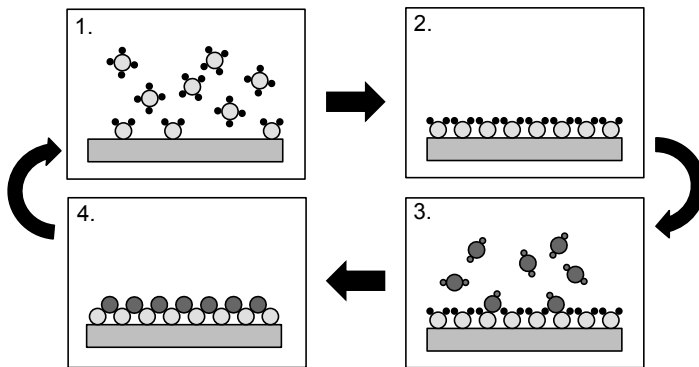

Figure 3.10. The ALD process.

This 4 step cycle is repeated until the desired film thickness is achieved, and the result is an amorphous film. The process is ideally linear with one monolayer of the film deposited in each cycle. Depending on the substrate this linearity is however often not achieved in the first cycles when the substrate material is still affecting the reaction.

One big advantage of the ALD process is that it is possible to coat very complex surfaces with a coherent film, and that very thin films can be achieved with high control over the coating thickness.

Depending on which type of film that is to be deposited, different precursor gases are used. In the case of the Al_2O_3 films made in this work the precursors are trimethylaluminum (TMA) and water.

One added advantage of the ALD technique for this particular application is that it has been proven to work at temperatures down to $33°C$ [42].

3.6.2 Plasma Enhanced Chemical Vapor Deposition

Plasma Enhanced Chemical Vapor Deposition (PECVD) is another standard thin film deposition technique. In the PECVD process the substrate is exposed to a flow of mixed precursors in gas phase, and the reactivity of the gases is enhanced by the creation of a plasma [43]. PECVD can thus be performed at lower temperatures than conventional CVD where the reactivity is thermally increased. This is why PECVD is a better choice for applications where the substrate is sensitive to high temperatures.

One possible disadvantage of the PECVD technique is that it could be difficult for the plasma to reach into the plastic cylinder used in the SAUNA system, and cover it with a uniform film.

Further details about the PECVD process, and the equipment used to produce the coatings tested in this work, can be found in Ref. [44].

4. Diffusion mechanism in the plastic scintillator

This chapter describes a study of the diffusion mechanism in the plastic scintillator material. The motivation for this work was to gain understanding of the mechanisms behind the memory effect, described in Section 3.5, and to explore saturation of the detector material with stable xenon, as a potential solution to the memory effect problem.

The work has not been published before but it was presented at the conference MARC IX (Methods and Applications of Radioanalytical Chemistry) in Kailua-Kona, HI, USA, in March 2012.

Our work is a continuation of a study performed by Health Canada [33], where they filled a plastic scintillator detector cell with stable xenon, to a little below atmospheric pressure, and then monitored the pressure in the cell at constant temperature for around 150 hours. They saw a pressure drop of around 5% which they interpreted as xenon dissolving in the polymer, and then diffusing out of the detector material.

We reproduced this measurement by filling a SAUNA plastic scintillator detector cell with stable xenon to around 0.9 bar, and then monitoring the pressure in the cell over time, at room temperature. The resulting pressure curve is shown in Figure 4.1. A pressure drop of around 5% is observed and the curve flattens out after around 100 hours. Both observations are consistent with the results presented in Ref. [33].
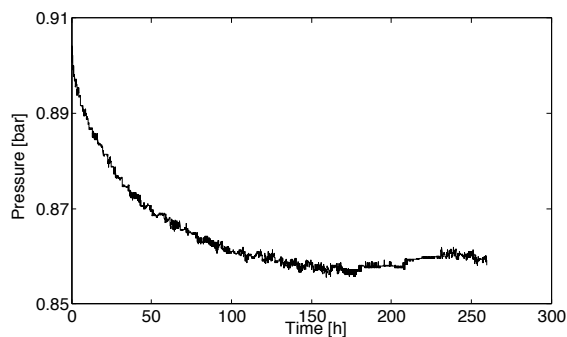

Figure 4.1. Xenon pressure in a SAUNA plastic scintillator detector cell monitored for around 250 hours.

Directly after the measurement shown in Figure 4.1 the detector cell was emptied, and filled again with stable xenon to the initial pressure of around

0.9 bar. The pressure was then monitored for another 100 hours, and this time no pressure drop was observed. This observation was interpreted as the detector material being saturated with xenon, and led to the idea that it might be possible to pre-expose the detector material to stable xenon, and in this way reduce the memory effect in the detector. This idea was tested, as described in Section 4.1. We also analyzed the pressure curve shown in Figure 4.1 in order to investigate if there is any theoretical support for the hypothesis of diffusion being the mechanism behind the memory effect. This part of the study is presented in Section 4.2.

4.1 Saturation of plastic scintillator cell

In order to test the saturation approach as a solution to the memory effect problem, a new detector cell was filled with stable xenon, and left for 500 hours at room temperature resulting in a pressure curve similar to the one in Figure 4.1. Immediately after the exposure the detector cell was emptied, and around 2.6 kBq of radioactive ^{133}Xe was introduced into the detector, together with helium up to a pressure of around 0.9 bar. The radioactive sample was left in the detector for around 7 hours, before being removed by pumping and flushing with helium.

The detector was mounted in a SAUNA laboratory system, and placed inside a NaI detector, as described in Section 3.2.2. The plastic scintillator cell and the NaI detector were used to do beta-gamma coincidence measurements of the activity in the detector cell during, and after the exposure to the radioactive gas.

Finally the memory effect ME was calculated as the ratio between the exposure activity (A_{expo}) and the residual activity (A_{resid}):

$$ME = \frac{A_{resid}e^{\lambda t_d}}{A_{expo}}, \tag{4.1}$$

where the factor $e^{\lambda t_d}$ is used to correct for decay of the residual activity during the time t_d between the start of the two measurements.

This procedure used to measure the memory effect is described in detail in Paper III, where it was used to study the memory effect in a coated plastic scintillator detector.

The resulting memory effect in this detector was determined to 2.9%, which is only slightly lower than the memory effect of 3-4% usually observed in normal detectors. It was thus concluded that saturation is not a viable solution to the memory effect problem. One explanation for the lack of memory effect reduction in the saturated detector, could be that there is a significant exchange of xenon atoms at the surface due to desorption and adsorption. This hypothesis is supported by the fact that no pressure drop was observed during the

exposure of the cell to the radioactive gas, indicating that there is a gas exchange taking place, rather than more xenon getting dissolved in the polymer.

4.2 Diffusion as the mechanism behind the memory effect

It is the common belief that diffusion is the mechanism behind the memory effect in the SAUNA detectors. We have used our pressure measurement to investigate if this gives any support to the diffusion hypothesis.

Under the assumption that the pressure drop in the detector is caused by xenon getting adsorbed in the polymer, and then diffusing through the material, we have tried to fit our pressure data to a solution to the diffusion equation.

4.2.1 Theoretical background

Gas permeation through polymeric systems (mostly membranes) is a widely studied topic, due to the use of polymers for, for example, packaging, gas separation and drug implants. Depending on the application the polymer should function as a diffusion barrier, have high selectivity, or high permeability.

In general the transport of gases through a polymeric membrane, separating two volumes with different gas pressure, is described by the solution-diffusion model [45, 46]. This is a three step process where the gas is first dissolved at the high pressure interface of the membrane, then diffuses through the bulk of the material, to finally desorb at the low pressure side of the membrane. The slowest process here is the diffusion which thus determines the time characteristics of the gas transport [45, 46].

The equilibrium amount of gas C dissolved in the interface is given by Henrys law:

$$C = Sp, \qquad (4.2)$$

where S is the solubility coefficient for the gas/polymer system, and p is the pressure on the membrane surface [47].

The flux J of gas atoms or molecules through the system is described by Fick's first law:

$$J = -D\frac{\partial C}{\partial x}, \qquad (4.3)$$

where D is the diffusion coefficient.

Equation 4.3 is only valid in steady state, when the concentration gradient in the membrane does not vary in time [48]. The concentration of gas atoms

in a homogeneous and isotropic polymeric membrane, as a function of both time t and penetration distance x can be described by Fick's second law:

$$\frac{\partial C(x,t)}{\partial t} = D\left(\frac{\partial^2 C(x,t)}{\partial x^2}\right) \tag{4.4}$$

Equation 4.4 is the one dimensional version of the standard diffusion equation which is valid for any system geometry:

$$\frac{\partial C(\vec{r},t)}{\partial t} = \nabla^2 C(\vec{r},t) \tag{4.5}$$

The diffusion and solubility coefficients are independent of concentration only for ideal systems where there are no interactions between the penetrating atoms, and where the interactions between the polymeric chains are constant [47]. This should be a good model for inert gases, such as xenon. The permeability P of a polymeric membrane is given by the product of the solubility and the diffusivity, $P = SD$.

For glassy polymers the situation is more complicated than the model described above due to the restricted movement of the polymeric chains (compared to rubbery polymers).

The gas sorption in glassy polymers is described by the dual-mode sorption model [49]. According to this model the gas can be dissolved in the polymer matrix in two ways, described as Henry's law dissolution (as above) and the additional Langmuir adsorption.

The Langmuir adsorption describes gas atoms or molecules trapped in pre-existing micro voids in the polymer matrix.

The two different populations of gas molecules in the polymer have different mobilities, and should therefore be described by multiple diffusion coefficients. The atoms or molecules adsorbed in microvoids tends to have lower mobility than the Henry's law dissolved gas.

4.2.2 Analysis of the pressure curve

Assuming that the pressure in the detector cell changes due to xenon diffusing into the detector material, the observed pressure drop can be related to the amount of xenon that have diffused into the plastic scintillator material. If this is the case, it should be possible to describe the shape of the pressure curve by a solution to the diffusion equation (Equation 4.5).

In order to simplify the analysis we treat our three dimensional problem as a one dimensional one.

In Figure 4.2 our simplified system model is illustrated. Here we assume that we have an infinite reservoir of xenon at constant pressure, in connection with an infinite piece of plastic material. The surface area of the xenon/plastic interface is the same as the surface area of the inside of the cylinder in our real system.
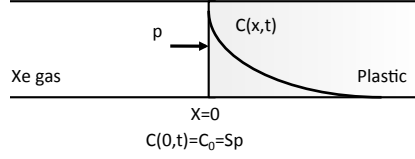
Figure 4.2. Illustration of the simplified diffusion model used in the calculations.

We also assume that there is no xenon in the plastic material at the start of the measurement ($t = 0$), and that at $t > 0$ the concentration at the interface ($x = 0$) is given by the equilibrium concentration according to Henry's law (Equation 4.2). We thus assume that the Langmuir type adsorption in negligible.

For this simplified geometry the three dimensional diffusion equation (4.5) reduces to the one dimensional case described by Fick's second law (4.4). One solution to this equation, with a boundary condition of fixed xenon concentration $C_0 = Sp$ at the interface, is given by [50]:

$$C(x,t) = C_0 \left(1 - erf\left(\frac{x}{\sqrt{4Dt}} \right) \right), \tag{4.6}$$

where the error function is defined as:

$$erf(u) \equiv \frac{2}{\sqrt{\pi}} \int_0^u e^{-s^2} ds \tag{4.7}$$

Equation 4.6 describes the evolution of the xenon concentration in the plastic material as a function of time t and penetration distance x. If assume that the gas in the detector cell contains only xenon, and that it behaves like an ideal gas, then the pressure in the detector cell may be expressed as a function of the xenon concentration in the plastic material:

$$p(t) = \frac{kT}{V} \left(N_0 - A \int_0^\infty C(x,t) dx \right), \tag{4.8}$$

where k is the Boltzmann constant, T is the temperature, V is the volume inside the detector cell, N_0 is the initial number of atoms in the gas in the cell and A is the surface area of the plastic. The integral term corresponds to the number of xenon atoms that have diffused into the plastic after a certain time t.

If we combine Equations 4.6 and 4.8, and use $C_0 = Sp_0$, where p_0 is the initial pressure in the cell, we have an expression of the pressure in the cell as a function of time, which we can fit to the measurement shown in Figure 4.1.

Since we assume infinite plastic material this function should only mimic our system for the first part of the measurement, before the xenon has gone through to the other side of our real finite plastic material. In this fit equation both the diffusivity D, and the solubility S are unknown.

As a starting point the solubility was set to a value found in the literature for polystyrene [33], which is a plastic similar to similar to the polyvinyltoulene in the plastic scintillator [51]. The solubility does not differ much from polymer to polymer compared to the diffusivity [51].

Using this solubility Equation 4.8 was fitted to the first 20 hours of our pressure measurement, with the result shown in Figure 4.3. The resulting value of the diffusivity was determined to $D = 1.03 \times 10^{-9}$ cm^2/s, a value of the same order of magnitude as the tabulated one for polystyrene [33].

With a diffusion coefficient of the order of 10^{-9} cm^2/s, the xenon reaches 1 mm into the plastic material (which is the real thickness of the plastic) after 20-30 hours, indicating that our simplified model should in fact be valid in this time frame.
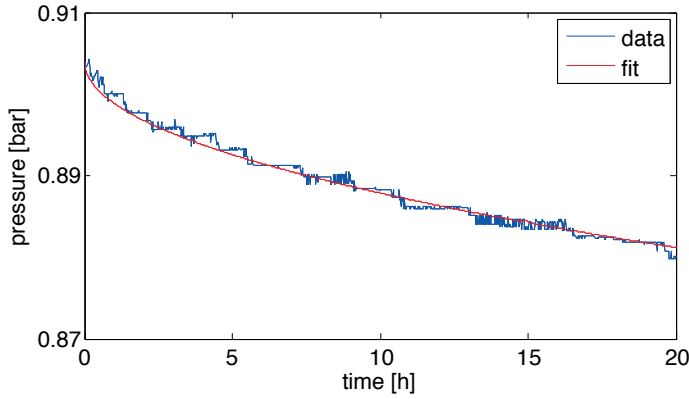

Figure 4.3. Pressure data and least squares fit of Equation 4.6.

If both S and D are free parameters it is not possible to find one single optimal set of values for both parameters, but rather a relation between the two. The top panel of Figure 4.4 shows the sum of squared errors of the fit function with respect to the pressure data, as a function of both parameters. There is a clear valley in the generated surface corresponding to the optimal relation between the solubility and the diffusivity.

The bottom panel in Figure 4.4 shows the logarithm of the optimal diffusivity as a function of the logarithm of the solubility, using values from the valley in the surface shown in the top panel of the same figure. It looks clear in the figure that the optimal value of log(D) is linearly dependent on log(S).
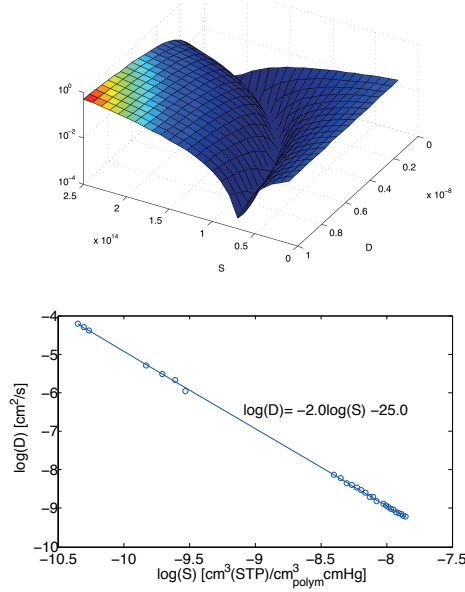
Figure 4.4. Top: Surface showing the sum of the squared errors of the fit function with respect to all pressure data points, as a function of *S* and *D*. Bottom: The optimal value of the diffusivity as a function of solubility. The points are taken from the surface above.

The conclusion from this part of the study is that it is possible to fit a solution to the diffusion equation to the first part of our pressure measurement. Furthermore it is possible to achieve a reasonable diffusion coefficient from this fit.

4.3 Conclusions

This study is an attempt to understand the mechanisms responsible for the memory effect in the plastic scintillator detectors used in SAUNA system. The pressure drop observed in the detector filled with xenon is interpreted as xenon being dissolved in the polymer and then diffusing into the material. This hypothesis was tested by fitting the data to a solution to a one dimensional diffusion equation, showing good agreement between the proposed model and the observed data, giving confidence in that diffusion is in fact a part of the mechanism behind the memory effect.

It was further seen that saturating the detector with stable xenon does not reduce the memory effect significantly, indicating that there is a significant exchange of atoms being adsorbed and desorbed at the surface.

It should be noted that a simplified model was used to study the diffusion in this study, and a number of approximations were performed when formulating the fit function.

A first extension of the analysis would be to include the second boundary condition of zero xenon concentration at $x = 1$ mm. By doing this it would be possible to use the whole pressure curve, and not just the first part as have been done in this study. An additional improvement might also be to include the Langmuir adsorption in the analysis and fit using multiple diffusion coefficients.

It should also be noted that our measurement was not designed to determine diffusivities and solubilities. There are standard measurement procedures that may be used to obtain more accurate values of the diffusivity and solubility of xenon in our plastic [47].

5. Coating of plastic scintillators to reduce the memory effect

The main approach investigated in this thesis, as a solution to the memory effect problem described in Section 3.5, is to coat the plastic scintillator with a material that is working as a xenon diffusion barrier. An important property of the coating is that it should not impair the resolution and efficiency of the detector.

The basis of this thesis (Papers I-III) is the investigation of transparent metal oxide coatings as gas diffusion barriers for the plastic scintillator detectors in the SAUNA system. Metal oxide coatings are standard coatings known to work as gas diffusion barriers in other applications [39, 40]. The transparency is an important property in order to preserve the resolution of the plastic scintillator detectors, as mentioned in Section 3.6.

Al_2O_3 coatings deposited with ALD, and SiO_2 coatings deposited with PECVD were chosen as candidate coating materials, since they both fulfill the desirable characteristics outlined in Section 3.6. The two coating techniques are briefly described in Sections 3.6.1 and 3.6.2.

In Section 5.1 in the present chapter, an evaluation of the potential of these two coating materials to work as xenon diffusion barriers on plastic scintillators is described, based on Papers I and III. Section 5.2 describes simulations and measurements conducted to assess the effect these coatings have on the resolution of the detector, based on Papers II and III.

The work presented in Papers I to III was conducted between 2009 and 2011 as a collaboration between FOI, Uppsala University (UU), and the University of Texas at Austin (UT). In Section 5.3 the continuation of the project since then is briefly summarized.

In addition to the study of transparent oxide coatings, a theoretical study of graphene as a diffusion barrier for this application was performed as part of this project. This study is described in Paper IV, and a brief summary of the paper is given in Section 5.4.

Finally, Section 5.6 contains an outlook describing a potential use for the results also in other applications.

This chapter will not describe in detail the calculations and experiments performed, but rather give a summary of the work done, and highlight the main results. For further details the reader is referred to Papers I-IV.

5.1 Evaluation of Al_2O_3 and SiO_2 as xenon diffusion barriers on plastic scintillators

This study was performed in two steps, where first several coatings of different thicknesses were deposited onto flat plastic scintillator samples, and the memory effect from xenon exposure of the samples was measured. These measurements are described in detail in Paper I, and the purpose was to identify a useful coating.

In the second step 425 nm Al_2O_3, which was the coating found to remove most of the memory effect, was deposited onto a complete plastic scintillator detector cell, and its performance was evaluated in terms of both memory effect, efficiency and resolution. This work is described in detail in Paper III.

5.1.1 Flat plastic samples

The measurements of the memory effect in the flat plastic scintillator samples were conducted both at FOI and at UT. The remainder of this section will focus on the measurements performed at FOI, and further details about the UT measurements can be found in Paper I (Sections 2.2.2 and 3.2), as well as in Ref. [44].

Al_2O_3 coatings of thicknesses between 20 and 425 nm, and SiO_2 coatings of thicknesses between 230 and 422 nm were evaluated at FOI. Further details about the samples and specific coating parameters can be found in Section 2.1 in Paper I.

The basic idea of the measurements performed at FOI was to expose the coated samples, as well as uncoated reference samples, to radioactive ^{133}Xe during 7 hours, and then measure the residual activity left in the samples after the exposure. The memory effect in each sample was calculated as the ratio between the residual activity and the exposure activity. The activity was measured using the SAUNA NaI(Tl) detector described in Section 3.2.2. The measurement procedure and experimental setup is described in detail in Section 2.2.1 in Paper I.

As explained in Section 3.1.1, ^{133}Xe decays through beta decay, with a high probability of an associated gamma ray of 81 keV. The activities were determined by analyzing this peak in the gamma spectrum measured by the NaI(Tl) detector (see Fig. 8 in Paper I).

The results from the memory effect measurements are summarized in Figure 5.1. It is seen that all coated samples have a lower memory effect than the uncoated ones. For the Al_2O_3 samples a trend of lower memory effect with increasing coating thickness is observed. The Al_2O_3 samples with a thickness of 425 nm have a memory effect of the same order of magnitude as a plain Al disc which was measured in order to determine the lower memory effect limit that can be measured using this technique. The memory effect in this sample is around a factor of 100 lower than what is seen in uncoated samples.

For the SiO$_2$ samples no apparent trend can be observed, and these coatings does not seem to work as good as xenon diffusion barriers as the Al$_2$O$_3$ coatings.

Shown in the figure is also the expected memory effect in a complete detector, which was determined by scaling with the difference in surface area between the real detector and the flat samples used in this experiment. For the uncoated samples this results in a memory effect of around 5% for the complete detector, which is in good agreement with what is usually observed in operational SAUNA systems (see Paper IV or Section. 3.5).

Further details and discussions about the results can be found in Sections 3 and 4 in Paper I.
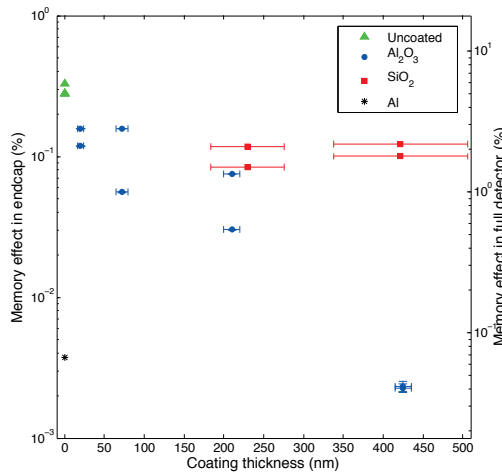

Figure 5.1. Results from the initial memory effect measurements using flat scintillator samples coated with Al$_2$O$_3$ and SiO$_2$. Shown is the memory effect in various coated samples, as well as 2 uncoated samples, and one plain Al disk used to estimate the lower limit of this measurement technique. The values are given as the percentage of the exposure activity left in the sample after evacuation of the radioactive gas from the test chamber. The left y-axis shows the measured memory effect in the sample, and the right y-axis shows the expected memory effect in a complete detector, obtained by scaling the values with the difference in plastic surface area between the two cases. The error bars in the y-direction take into account the uncertainties in the peak areas, which are given by counting statistics, and the uncertainties in the dead time correction. The error bars are included, but not visible, for all data points. The uncertainties are discussed in further detail in Paper I. The error bars in the x-direction take into account the uncertainties in the determination of the coating thickness. The larger uncertainties for the SiO$_2$ samples compared to the Al$_2$O$_3$ samples are due to different techniques used to determine the coating thickness of the two materials. Note that the y-axis is in logarithmic scale.

5.1.2 Complete detector

Being identified as the most promising coating, 425 nm Al_2O_3 was deposited onto a complete cylindrical plastic scintillator cell. This detector was mounted in a SAUNA system, as described in Section 3.2.2, and the memory effect in this detector was measured as described in Paper III.

The measurements were conducted similarly as for the flat coated samples, with the exception that the detector could also be operated in beta gamma coincidence mode. In Figure 5.2 the resulting spectra of the exposure, and the residual activities are shown, as measured in beta-gamma coincidence mode using the coated plastic scintillator and a NaI(Tl) detector.
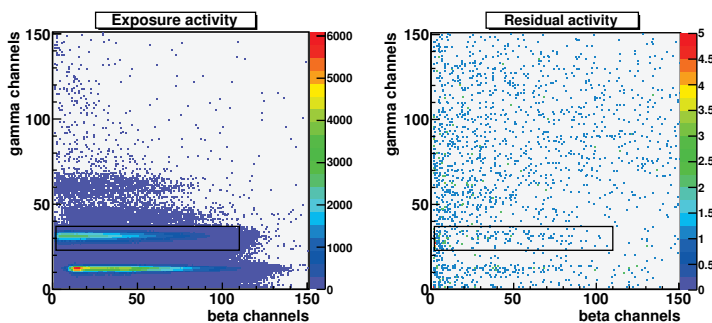

Figure 5.2. Beta-gamma coincidence spectra measured using the coated plastic scintillator detector cell. The left panel shows the exposure activity of ^{133}Xe, and the right panel shows the residual activity left in the detector after evacuation of the gas sample. It should be noted that the exposure activity was measured during 7 hours, while the residual activity was measured during 44 hours. The two spectra shown in the figure are not scaled to the same live time. Note also that the scales are different in the two spectra.

It is clear from this picture that the memory effect in the coated detector is indeed very small. The activities used to calculated the memory effect in this setup were determined by looking at the number of counts in the ROI indicated in the figure. This region contains the counts corresponding to the beta decay of ^{133}Xe, in coincidence with a 81 keV gamma ray (see Section 3.2.1). A detailed description of the analysis of the spectra can be found in Section 2.2.2 in Paper III.

The memory effect for this complete coated detector was determined to around 0.002%[1], which is a factor of 1000 smaller than what is usually observed in uncoated detectors. This is an even higher memory effect reduction than anticipated from the experiments with the flat samples, which showed a reduction of a factor of 100. This discrepancy is discussed in Section 4.2 in

---

[1]When measured in beta gamma coincidence mode. Measurements using only the NaI(Tl) detector as in Paper I were also conducted, yielding a memory effect of 0.0044%.

Paper III, and its reason is believed to be that the major part of the memory effect measured in these coated samples is related to other parts of the experimental setup rather than the actual plastic material, such as the optical glue used to assemble the cell.

5.2 Light collection and resolution of a coated detector

For the coating approach to be a feasible solution to the memory effect problem, it is important that the energy resolution of the detector is not impaired by the coating. This is especially true since the detection system needs to be able to distinguish the two CE peaks from ^{131m}Xe and ^{133m}Xe at 129 and 199 keV respectively, as shown in Figure 5.3.
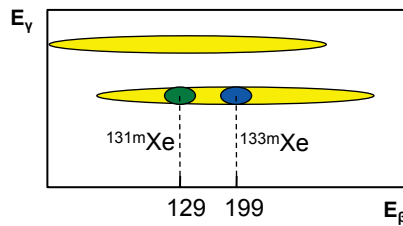

Figure 5.3. Schematic picture of a beta-gamma coincidence spectrum containing conversion electrons from ^{131m}Xe (green) and ^{133m}Xe (blue), on top of ^{133}Xe in yellow (compare to Figure 3.3 in Section 3.2.1).The electron energies are given in keV on the x-axis.

An important part of this project has thus been to evaluate the impact that a coating would have on the detector resolution. In order to address the resolution issue at an early stage in the project, as well as to find potential restrictions and recommendations for coating parameters, a study of the light collection in the SAUNA beta detector was performed.

In this work, the energy resolution of the SAUNA beta detector is assumed to be dominated by photoelectron statistics, as well as variations in the detector response depending on the spatial position of the particle interaction in the detector. This is often the case for detectors with complex shape, as mentioned in Section 1.5.3. Both these factors are governed by the light collection in the detector, which may be studied independently from the rest of the detector setup, both through simulations and measurements.

Other possible contributions to the resolution of this particular detection system, apart from those listed in Section 1.5.3, may be:

- Mismatching between the two PM-tubes used to convert the light signal from the scintillator. Given equal quantum efficiencies of the two PM-

tubes, and spatial symmetry in the light collection efficiency, the gain of the PM-tubes should ideally be the same [52].

- Self absorption in the xenon gas, due to interactions between the radiation to be detected and the xenon atoms. Normally the xenon sample in the cell is around 1.3 cm^3 of which the major part is stable xenon. The resolution of the 129 keV peak has been measured for such "normal" sample, containing a small amount of ^{131m}Xe, as well as a sample without stable xenon but with the same radioactive content. The difference in the CE resolution at 129 keV between the two samples was measurable, but only 1%.

These contributions, as well as electronic noise and drifts in the operating parameters are assumed to be small compared to photoelectron statistics and the spatial variations in detector response.

The study of the light collection is described in Paper II, and the main part of the paper is dedicated to Monte Carlo simulations of the light collection efficiency in coated and uncoated detectors. The purpose of the study was to investigate how properties like the surface quality of the plastic material and the coating, the coating thickness, and the refractive index of the coating affected the light collection, and hence the detector resolution.

The simulations were performed using the Monte Carlo code Detect2000 [53], which tracks individual photons as they travel through a user defined geometry. By specifying refractive indices and absorption lengths of all materials, as well as optical properties of all surfaces, light losses due to absorption or escape can be simulated. Photons are recorded as detected if they reach a surface defined as a photocathode. If the quantum efficiency of the photocathode is known it is then possible to determine the number of photoelectrons created for a given number of produced scintillator photons.

The surface models used in the simulations were the POLISH and GROUND models that are implemented in Detect2000 [53]. When a photon encounters a surface it is first determined if it is to be reflected, or transmitted into the next medium. The probability for reflection is determined using Fresnel's formula:

$$R = \frac{1}{2}\left[\frac{sin^2(\theta_i - \theta_t)}{sin^2(\theta_i + \theta_t)} + \frac{tan^2(\theta_i - \theta_t)}{tan^2(\theta_i + \theta_t)}\right], \tag{5.1}$$

where θ_i is the angle of incidence and θ_t is the transmission angle. The angles are defined with respect to the normal of a local micro-facet.

For the POLISH surface model this micro-facet is always parallel to the macro surface, and thus defines a totally smooth surface. The GROUND surface model represents a rough surface, and the normal of the micro-facet is sampled from a Lambertian distribution around the normal of the macro surface.

In both cases the complementary probability of transmission is given by $T = 1 - R$. The transmission angle is determined from Snell's law of refraction, and the photon can still be internally reflected if the angle of incidence is smaller than the critical angle for total internal reflection, defined in Eq. 1.8.

If the neighboring medium is vacuum, an external reflection coefficient can be defined, giving the probability that an escaped photon is reflected back into where it came from. The reflection angle is sampled from a Lambertian distribution, and the reflector is thus diffuse. This reflection coefficient can be used to simulate an external diffuse reflector, in this work the teflon tape that is wrapped around the real detector.

It should be noted that it is not likely that the real detector is well described by either the POLISH or the GROUND surface models, but its roughness is probably somewhere between these two simulated extremes. This was also confirmed by comparing the calculated resolutions for the uncoated detector with real measurements, as explained in Paper II. The purpose of the simulations was not to exactly reproduce the performance of a real detector, but rather to investigate if the light collection efficiency would be impaired by a coating. It is believed that this was captured despite the simplified surface models.

Details regarding the implemented geometry and the setup of the simulations can be found in Section 2.1 in Paper II. The basic idea was to study the light collection efficiency (defined in Section 1.5.3) as a function of starting position of photons in the detector geometry. The absolute value of the light collection efficiency captures the photoelectron statistics and the spread in the efficiency with respect to photon staring point (i. e. interaction point of the incoming radiation) captures the spatial variations in detector response. The two contributions can be combined to a total detector resolution, as described in Section 2.1 in Paper II, and Section 1.4.1 in this thesis. The resulting resolution will be an underestimation of the real resolution of the detector, since not all contributions are accounted for, as mention in the beginning of this section.

The main conclusions drawn from the simulations are:

- The light collection efficiency is highly dependent on the surface quality of both the plastic scintillator, and the coating. This is true both when it comes to the absolute efficiency, and the spatial variations.
- In the case of smooth surfaces the resolution is dominated by the photoelectron statistics, and when rough surfaces are involved spatial variations is the dominating contribution.
- A coating with a rough surface impairs the light collection, regardless of the quality of the plastic surface. However, if a smooth coating is achieved on a rough plastic surface, the light collection can be improved by the coating.
- A good optical match between the refractive indices of the plastic scintillator and the coating is important. Furthermore, it is preferable that
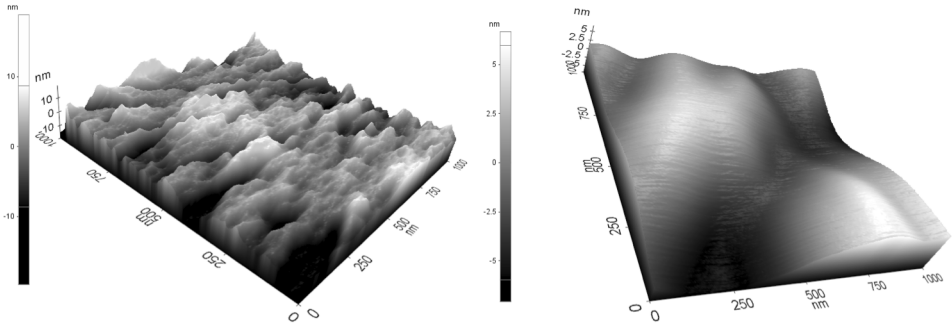
Figure 5.4. AFM picture of the surface of a plastic scintillator sample before (left) and after (right) it was coated with 210 nm Al_2O_3

> the refractive index of the coating is higher than the one of the plastic, rather than lower.
> - For the coating thicknesses below 1 μm simulated here, the light collection efficiency is not significantly dependent on the coating thickness.

The most important property to consider was found to be the surface quality of the coating, and a smooth coating on a rough plastic surface may even improve the light collection. The light collection efficiency is not expected to be significantly impaired if a smooth coating with a refractive index close to the one of the plastic scintillator can be achieved.

The surface roughness of a flat plastic scintillator sample was later studied both before, and after, being coated with Al_2O_3, using Atomic Force Microscopy (AFM) [54]. Figure 5.4 shows the results from these measurements, and it is clearly visible that the coating has a smoothening effect on the scintillator surface. This is very promising from a light collection point of view.

At the end of this project one complete detector was coated with 425 nm Al_2O_3. The resolution of this detector was measured twice, by introducing ^{131m}Xe into the detector, and subsequent analysis of the measured 129 keV CE peak (see Section 2.1 in Paper III). In Figure 5.5 the resulting resolutions are shown, together with the 129 keV CE resolutions in operational SAUNA systems. The IMS systems are required to have a resolution no larger than 40 keV at this energy [21]. The CE resolution at 129 keV of the complete coated detector was around 33 keV in both measurements. This value is below the mean resolution of uncoated detectors, and within the resolution interval presented by these.
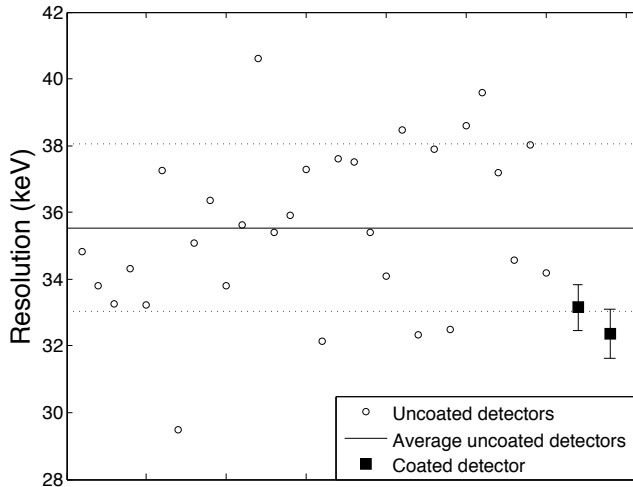
66

Figure 5.5. The electron resolution at 129 keV of all SAUNA detectors installed in the IMS in 2011, and two measurements of the corresponding resolution of the coated detector cell. The dotted lines show the one σ interval around the average resolution of the uncoated detectors.

5.3 Continuation of the project

In Sections 5.1.2 and 5.2 it was shown that it is indeed possible to achieve a significant memory effect reduction using Al_2O_3 coatings, without impairing the resolution of the detector. However, as mentioned in the conclusions of Paper III, some degradation of the coating over time has been observed for the coated detector discussed in this chapter. This degradation was manifested as an increased memory effect around 6 months after coating. It was also later seen that the coating started to flake off.

The plan is still to incorporate Al_2O_3 coated plastic scintillator detectors in the SAUNA systems that are part of the IMS network. However, before this can be done the reproducibility and the long term performance of the solution needs to be ensured. The radioxenon systems in the IMS are often located at remote locations, and it is necessary that they can work for longer periods of time without requiring maintenance.

Because of this, further studies are currently being conducted at FOI and at Scienta SAUNA Systems, in collaboration with the coating company Nanexa AB. This is done outside the work of this thesis, and the follow-up of the progress reported here is based on a personal communication with FOI [55].

Additional detectors have been coated, presenting a low memory effect and good resolution, but with the same problem of degradation in time as the initial one.

The reason for the degradation is believed to be cracking of the film due to residual water in the coating. The plastic surface is hydrophobic, which in combination with the low temperature of the coating process (45°C), may cause formation of Al_2O_3 islands on the surface, containing residual water precursor molecules. The residual water in the film may cause cracking and degradation in time due to movement of water molecules within the film. This island type growing of the film may also be an explanation for the need for a rather thick coating of 425 nm to remove the major part of the memory effect, since the whole plastic surface may not be covered by the thinner coatings.

To obtain a higher quality film, work has been conducted to make the plastic surface hydrophilic instead, and a pre-treatment (surface activation) has been found that, in combination with a higher coating temperature (just below the softening point of 70°C of the plastic material), results in a low memory effect already with a 100 nm coating. No difference was observed between 100 nm and 425 nm for this new coating procedure.

However, the surface activation seem to cause degradation of the detector resolution. Work is currently being conducted in order to come to terms with this issue. The ideal situation would of course be to be able to activate the plastic surface without degrading the resolution. It is also planned to polish all detectors before activation and coating, in order to maximize the chances of a sufficiently high resolution. As was pointed out in Paper II and Section 5.2 a smooth plastic surface may significantly improve the detector resolution, and with a better starting point some degradation due to the pre-treatment may be acceptable.

Tests will also be conducted with another plastic scintillator material, with similar properties as BC-404, but with a higher softening point of 100°C, which would allow a higher coating temperature and hopefully a higher quality coating.

5.4 Graphene

Paper IV presents a theoretical study of graphene as a xenon diffusion barrier in this application. Graphene is a monolayer of carbon atoms that are densely packed in a honeycomb pattern. This material is known to be impermeable to much smaller gas atoms than xenon, such as helium [56].

The purpose of this study was to investigate the potential of various small graphene flakes to work as a diffusion barrier. The reason being the difficulties of fabricating and handling large are graphene sheets. Defects in the form of rips were introduced, and the diffusion barrier properties of ripped graphene sheets were studied, as a function of rip width.

The study was performed using Density Functional Theory (DFT) which is a method based on the fact that the total (ground state) energy of an electronic system can be determined from the charge density in this system [57, 58]. By

calculating the electronic structure, i. e. solving the eigenvalue problem and obtaining the eigenstates (electron energies) and eigenfunctions (wave functions), the total energy and charge density can be determined. From this a number of physical properties can be understood. The electronic structure is calculated by solving the so called Kohn-Sham equation, which is a Shrödinger type equation, for all the electrons in the system.

The model system in this work consisted of 128 Carbon atoms and one xenon atom placed at different distances from the graphene surface. The surface contained a rip of Stone-Wales type, described in Ref. [59]. The distance h of the xenon atom from the graphene surface was varied as well as the width rw of the rip. For each $rw - h$ configuration the system was relaxed and the total energy was calculated.

The results showed that regardless of rip width, the total energy of the system increases as the xenon atom is moved closer to the surface.

For the widest rip studied, of 7 Å, the xenon atom would need a kinetic energy of 0.2 eV in order to overcome the diffusion barrier and pass through the graphene sheet. To put this in perspective, one can compare it to the average kinetic energy of an atom in gaseous phase given by, $E_{av} = \frac{3}{2}k_BT$, where $k_B = 8.62 \times 10^{-5}$ eV/K is the Boltzmann constant, and T is the temperature of the gas in Kelvin. At room temperature ($T = 300$K) this average energy is around 0.038 eV. It is thus quite unlikely that a xenon atom could overcome the 5 times higher diffusion barrier for the 7 Å wide rip.

In addition, it was found that intermediate rips self healed when approached by the xenon atom.

The conclusions from this study was that, from a theoretical point of view, a defect graphene sheet would indeed work as a xenon diffusion barrier. It is however not yet straightforward how to practically attach the graphene to the plastic scintillator cell, which is why no experimental tests of this potential solution have been performed so far.

5.5 Conclusions

In Section 5.1 it was concluded that it is possible to achieve a significant (factor of 1000) reduction of the memory effect in the SAUNA plastic scintillator detectors, by means of Al_2O_3 surface coatings, deposited using low temperature ALD.

It was further shown in Section 5.2 that such coating does not impair the energy resolution of the detector significantly. These conclusions are however based on measurements on one single coated plastic scintillator detector, and further studies have shown that the coatings are reproducible, but that there is a problem of degradation over time. This problem is hoped to be solved by activation of the detector surface before coating to make it hydrophilic, in combination with film deposition at higher temperature, as discussed in Sec-

tion 5.3. One explanation for the need for a rather thick coating to significantly reduce the memory effect may be due to island growing of the film because of the hydrophobicity of the plastic in combination with low coating temperature. Another potential explanation, of xenon being adsorbed in surface defects in the Al_2O_3 film, is explored by means of molecular dynamics simulations in Chapter 6 and Paper V.

An additional interesting observation from the study is the importance of a smooth detector surface when it comes to detector resolution, and that it seems to be possible to improve the resolution by applying a smooth film onto a rough detector surface.

5.6 Outlook

Even though xenon diffusion into plastic scintillators may seem like a problem present in a very small number of applications, the results presented in Paper I-III leads to the idea that this technique could be used also in other detector applications. To add a protective coating to the detector material could potentially solve a number of problems known in current detector systems, such as hygroscopicity and degradation due to uptake of atmospheric gases. The fact that the light collection does not seem to be impaired, and could even be improved, also makes this something that might be interesting also for other types of scintillators.

There are for example a number of crystalline inorganic scintillators that are hygroscopic, which means that they easily absorb and gets damaged by water. These scintillators typically needs to be placed in air tight containers to be protected from humidity in the air. These hygroscopic materials include both standard crystal scintillators like CsI(Tl), CsI(Na) and Na(Tl) [4], as well as recent developments. New detector materials include the high resolution scintillators $SrI_2(Eu)$, $LaBr_3(Ce)$ and $LaCl_3(Ce)$ [60, 61, 62], which are very promising when it comes to light yield but have the disadvantage of being hygroscopic.

Other detector materials may also be able to withstand higher coating temperatures than the plastic used in the SAUNA system, and the geometries are often less complex than the cylindrical shape of this detector. This puts less restriction on potential coating techniques and may increase the probability of achieving high quality films. There are also various other standard metal oxide coatings used as gas diffusion barriers apart from Al_2O_3, including SiO_2, MgO, TiO_2 and ZnO, with a spectrum of refractive indices between 1.5 and 2.1, making the possibilities of finding working solutions for individual detectors even greater.

6. Molecular dynamics simulations of the Al$_2$O$_3$-Xe system

In Chapter 5 it was shown that a rather thick coating of 425 nm was needed in order to achieve a large reduction of the memory effect. It was also observed that the plastic scintillator material contained surface imperfections in the form of scratches (see Figure 5.4).

One potential explanation for the smaller memory effect reduction for the thinner films may be that the surface imperfections on the plastic are not completely filled up by the thinner coatings. This may in turn lead to surface imperfections also on the resulting Al$_2$O$_3$ surface, which may act as adsorption sites for the xenon atoms.

It is not probable that this effect is the whole reason for the order of magnitude difference in memory effect between the 210 nm films and the 425 nm films observed in Figure 5.1, but it might be part of the explanation. Another explanation discussed in Section 5.3 was incomplete coverage of the plastic surface due to island growing of the film.

In order to investigate if this hypothesis could be true, the molecular dynamics study described in Paper V was performed.

In Section 6.1 of this chapter the method of molecular dynamics is described, and in Section 6.2 the work presented in Paper V is summarized.

6.1 Molecular dynamics

Molecular dynamics is a method that is used to study the behavior of gases, liquids and solids on an atomic or molecular scale, using computers.

The power of the method is increasing with improved computers, and today it is possible to model systems containing many millions of atoms, forming systems on the micrometer scale.

For classical molecular dynamics the time evolution of an atomic system is studied by solving Newtons equations of motion for all the atoms in the system.

Newtons second law relates the net force $\vec{F}_i$ acting on atom i, to the mass m_i and acceleration $\vec{a}_i$ of this atom:

$$\vec{F}_i = m_i\vec{a}_i \tag{6.1}$$

Another way that the conservative forces can be expressed is as a function of the potential energy Φ of the system:

$$\vec{F}_i = -\vec{\nabla}\Phi(\vec{r}_1, \vec{r}_2, \ldots, \vec{r}_N) \tag{6.2}$$

The potential energy Φ depends on the positions $\vec{r}_i$ of all atoms, and the force acting on atom i can thus be determined from the gradient of the potential with respect to the displacement of this atom.

The combination of Equations 6.1 and 6.2 yields the following equation of motion for each atom in the system:

$$-\vec{\nabla}\Phi = m_i \frac{d^2\vec{r}_i}{dt^2} \tag{6.3}$$

The potential function depends on the positions of all the atoms in the system, and assuming pairwise additivity is often a valid approximation. The potential function can then be taken as the sum of isolated pair interactions:

$$\Phi(\vec{r}_1, \vec{r}_2, \ldots, \vec{r}_N) = \sum_{i > j} V_{ij}(\vec{r}_i j), \tag{6.4}$$

where $\vec{r}_{ij} = \vec{r}_i - \vec{r}_j$ and V_{ij} is a known pair potential function describing the interaction between atom i and j [63].

The basis of molecular dynamics is to integrate Equation 6.3 for all the atoms in the system in order to obtain the atomic positions and velocities as a function of time. To do this one needs to know the pair potential function of the system, which will be described in more detail in Section 6.1.1, and initial conditions, usually the positions and velocities of all atoms at $t = 0$.

It is however not possible to solve the equations analytically, which is why numerical integrators are used in molecular dynamics. There are a number of different integration algorithms, of which the most common one is the Verlet algorithm [63] and [64].

Molecular dynamics is a deterministic method in the sense that atomic positions at a given time are determined from their previous positions. The method is coupled to statistical mechanics in the way that properties of the system can be obtained from these atomic trajectories.

In statistical mechanics one studies the macroscopical behavior of a system by looking at it from a molecular, or atomic, point of view. The microscopic state of a system is determined by the positions and momenta of all particles in this system. An ensemble is the collection of all possible microscopic states of a system that leads to the same macroscopic state. Ensemble averages of properties of such system can be calculated by averaging over all possible microscopic states in the ensemble. This is however very difficult to do due to the large number of possible states.

In molecular dynamics one studies the time averages of properties instead of the ensemble averages. This approach is based on the ergodic hypothesis

which states that if the number of states included in the time average is large enough, the time average equals the ensemble average [64].

A typical molecular dynamics simulation starts from an initial system configuration of atomic positions and velocities. New positions a short timestep ahead are determined by applying Newtons equations of motion, and trajectories of each atom are obtained in this way. Thermodynamic averages are calculated from these trajectories according to:

$$\langle A \rangle = \frac{1}{M} \sum_{m=1}^{M} A(\vec{p}^{N}, \vec{r}^{N}), \tag{6.5}$$

where M is the number of time steps in the average, and $\vec{p}^{N}$ and $\vec{r}^{N}$ are the momenta and positions of all N atoms in the simulation.

Usually the simulation starts with an equilibration phase where thermodynamic and structural properties are monitored until stability is reached. The second step is then usually a so called production phase, where the system configuration (positions and velocities of all atoms) is regularly output to a file. These configurations can then be used to calculate additional properties (time averages) of the system [64].

The advantage of molecular dynamics is that the only input needed is the potential function describing the interatomic or intermolecular interactions, and the initial positions and velocities of each atom. No other assumptions are made about the process or property that is to be studied, and the simulation can be thought of as an experiment in this sense.

There are however also a number of limitations of the method as described in for example Ref. [65]:

- The classical molecular dynamics method treats atoms as classical objects, and does not take into account quantum effects in the system. The atoms are treated as point particles at the position of the nucleus, and the electrons are fixed with respect to the nucleus and not taken into account explicitly. Some potentials do however take into account that the electrons may move with respect to the nucleus.
  The way of treating atoms as point particles have been shown to work well for all but the lightest atoms where quantum effects can become significant. An alternative to the classical molecular dynamics is quantum, or first principles, molecular dynamics where the valence electrons of each atom are treated with quantum mechanics, and the ions formed by the nucleus and inner electrons are treated classically.
- Molecular dynamics rely heavily on the use of good potential energy functions, which determine the dynamics of the system. Developing correct molecular dynamics potentials is often a great challenge. The potentials should mimic the real system without being to complicated and slow down the calculations, and there is often a trade off between these two requirements.
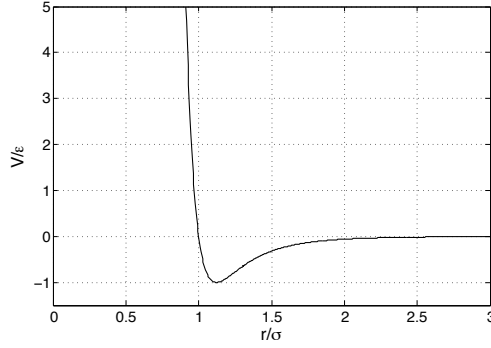
Figure 6.1. Shape of the Lennard-Jones potential. The potential is zero when $r = \sigma$, and the minimum potential is given by ε

6.1.1 Potentials

One of the simplest potentials used in molecular dynamics is the Lennard-Jones potential, which despite its simplicity has been shown to model the interaction between inert atoms, such as the noble gases, well. It is also often used to model also more complex systems due to its computational simplicity. The Lennard-Jones potential function is given by [66]:

$$V_{LJ} = 4\varepsilon \left[\left(\frac{\sigma}{r} \right)^{12} - \left(\frac{\sigma}{r} \right)^{6} \right], \tag{6.6}$$

where r is the distance between the two atoms, and σ and ε are parameters depending on the type of atoms in the system.

The shape of the Lennard-Jones potential is shown in Figure 6.1. One can see that the potential is zero when the interatomic distance $r = \sigma$, and that the minimum potential is given by ε. The value of ε thus determines the strength of the interaction between the atoms.

The potential consists of a repulsive term $\left(\frac{\sigma}{r} \right)^{12}$ and an attractive term $-\left(\frac{\sigma}{r} \right)^{6}$. The repulsive term dominates at short distances and is due to overlapping electron orbitals at such short distances. Due to the Pauli exclusion principle this overlap drastically increases the potential energy [66]. At longer distances the attractive term dominates, modeling the weaker Van der Waals force. When two inert gas atoms are brought together they can induce dipole moments in each other, which results in an attractive force.

For ionic systems, such as our Al_2O_3 system, the Lennard-Jones potential models the behavior of the atoms very poorly. There is a need for a potential

that take into account also the electrostatic interaction between the charged atoms.

For our system we used a potential of the form:

$$V(r_{ij}) = \frac{q_i q_j}{r_{ij}} - \frac{C_i C_j}{r_{ij}^6} + D(B_i + B_j) \exp\left(\frac{A_i + A_j - r_{ij}}{B_i + B_j}\right), \qquad (6.7)$$

where q_i and q_j are the effective charges of atom i and j respectively, and r_{ij} is the interatomic distance. The first term describes the repulsive Coulomb interaction between the charged atoms. The second term represents the Van der Waals force, and the last term is the repulsive force. D is a standard force constant and equals 4.184 kJ Å^{-1} mol^{-1}, A is the repulsive radius, B is the softness parameter , and C the Van der Waals coefficients. The exponential form of the repulsive term has been shown to represent the repulsive interaction for ions more accurately than the $(1/r)^{12}$ term used for the inert gases.

This potential was formulated by Matsui [67]. It has previously been used to model liquid Al_2O_3 [68], amorphous Al_2O_3 [69, 70], and amorphous Al_2O_3 surfaces [71].

In addition to the ones used in this work there are a large number of potentials used to model other types of systems. To model metallic systems, which require a more explicit treatment of the electrons compared to ionic systems, the Embedded Atom Model (EAM) is used [64]. Covalent systems have their own potentials, and there are even potentials where electrons are allowed to move between atoms and chemical reactions are treated in the simulations.

The size, time and length scales that are possible to simulate using molecular dynamics depend heavily on the complexity of the potentials that are used.

6.1.2 LAMMPS

LAMMPS (Large-scale Atomic/Molecular Massively Parallel Simulator) is a classical molecular dynamics code described in [72, 73], and it is the code that was used in the work presented in this chapter, and Paper V. The code is distributed by Sandia National Laboratories as open source and can be downloaded from [72]. It is designed to run efficiently on parallel computers, and can be used to model ensembles of particles in liquid, solid or gaseous state.

6.1.3 Radial distribution functions

One tool that is commonly used to characterize the structure of an atomic system is the radial distribution function (RDF). The radial distribution function $g(r)$ gives the probability of finding an atom at the distance r from another atom, compared to the corresponding probability if all atoms were uniformly distributed in the simulation box [72]. If $g(r)$ is equal to one this means that

the probability of finding an atom at this distance is just as high as if the atomic distribution was completely uniform.

The RDF has different features depending on the structure of the system. An ordered structure results in peaks at given distances, and a disordered structure have a flat appearance. For crystals one can see an infinite number of sharp peaks, where the heights and locations of these peaks depend on the lattice structure of the crystal. For low density gases the function is featureless since all distances are equally probable. Liquids and amorphous solids show characteristics of both a crystal and a gas. At short range there are a number of peaks, but at long range there is disorder and the function flattens out around one [64, 63]. The locations of the short range peaks contain information of the binding between the atoms.

From the radial distribution function one can extract another quantity, the average coordination number which is obtained by integrating around the first peak in the radial distribution function. It gives the average number of nearest neighbor atoms for each combinations of two atoms. The average coordination number is calculated according to:

$$n_{\alpha\beta}(R) = 4\pi\rho_\beta \int_0^R g_{\alpha\beta}(r)r^2 dr, \tag{6.8}$$

where R is a cutoff taken as the position of the minimum after the first peak, and ρ_β is the number density of atomic species β.

The radial distribution functions and coordination numbers are used to characterize the amorphous structure generated in Paper V.

6.2 Our study

The molecular dynamics study presented in Paper V consist of four main steps which are briefly summarized in this section.

6.2.1 Bulk amorphous Al_2O_3

In the first step a bulk amorphous sample was generated using the so called melt and quench method [69, 74, 70]. Here a crystalline structure is heated to form a disordered liquid. The system is then rapidly cooled in order to preserve the disorder from the liquid, but in a solid phase.

Our simulations were performed in the NVT and the NVE ensembles, where the volume of the system is fixed and the pressure is allowed to fluctuate when the temperature of the system is changed.

In the first part of the simulation the volume had one fixed value, resulting in a density corresponding to a liquid phase at the desired temperature. When going from the liquid phase to the solid phase, the volume was rescaled to a

new fixed value in order to obtain a density known to correspond to a stable amorphous phase.

A more realistic way of doing the simulations would be to use the NPT ensemble instead, where the pressure is fixed at atmospheric pressure and the volume is allowed to change with temperature. However, as mentioned in Ref. [69] and showed in Ref. [74] the cooling rate when going from liquid to solid phase may affect the characteristics of the resulting structure significantly. For slow cooling rates at constant pressure one may even end up with a crystalline structure. The density of the resulting structure was also shown to depend on the cooling rate used.

Because of this, we used an ensemble with fixed volume so that a system with the desired density could be achieved more easily.

Further details on the setup of the simulations, as well as radial distribution functions and coordination numbers for the resulting amorphous sample can be found in Paper V.

6.2.2 Amorphous Al_2O_3 surface

From the bulk sample a surface was created by simply extending the simulation box in one direction, creating a vacuum above the bulk sample. The formed surface was then allowed to relax.

Two types of surfaces were created. A flat surface generated as above, and a surface containing scratches, in the form of 10 Å wide and 10 Å deep valleys which were created by removing atoms from the surface, and allowing the structure to relax (see Figure 6.2).
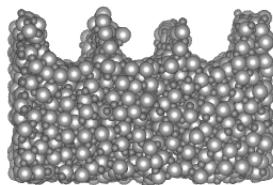

Figure 6.2. Image of the scratched surface. The valleys are 10 Å wide and 10 Å deep.

Details regarding the surface generation can be found in Paper V. The structure of the flat surface was characterized and compared to Ref. [71]. As in previous work the RDF's for the surface indicated a preference for edge sharing of the AlO_4 tetraheda at the surface, compared to the bulk.

6.2.3 Adsorption energies

The likelihood of xenon being adsorbed on the Al_2O_3 surfaces described in the previous section, was studied by looking at the adsorption energies of xenon on the surface. This was done by placing a xenon atom at various positions above the Al_2O_3 surface, and then calculating the total energy of the system at 0 K. The xenon atom was moved in a 3D grid with 0.5 Å spacing in every direction. The potential energy of the system was then compared to the potential energy of the system without xenon. The resulting energy differences give an idea of the adsorption energies at the surface. The difference is calculated in such way that a negative value means that the system energy is lowered by the presence of xenon at that position, and the zero point is set to the system energy without xenon.

In Figure 6.3 the minimum potential energy of the system, expressed as the change in energy by the presence of xenon, is shown for every xy-position. The minimum energy value has been filtered out from all tested distances from the surface, for every xy-position. These minimum potentials give an idea of potential adsorption sites on the surface, and the magnitude of the energy changes are interpreted as adsorption energies.
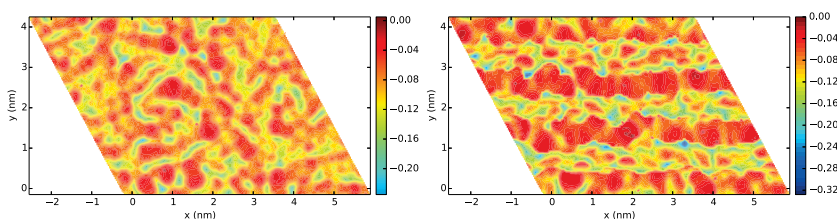

Figure 6.3. The potential energy surface for the flat (left) and scratched (right) Al_2O_3 surface. The colors show the minimum potential energy in eV for each xy-position above the surface. Blue regions are those where the adsorption energy is highest, and thus the most probable adsorption sites. For the scratched surface it is seen that these adsorption sites are located in the valleys constituting the scratches.

Figure 6.4 shows the distributions of minimum potential energies for the surfaces shown in Figure 6.3.

In the two figures one can see that there are a significant number of sites on both surfaces where the adsorption energy is higher than 0.1 eV. For reference, this energy is 4 times higher than $k_B T$ at room temperature which is 0.025 eV, indicating that it is indeed a high probability that a xenon atom may remain adsorbed to the surface at this temperature.

By comparing the two surfaces it is seen that the scratched surface have deeper energy valleys, with higher adsorption energies, compared to the flat surface. These energy valleys are located in the scratches, as seen by comparing Figure 6.3 and Figure 6.2, and the adsorption of xenon is thus stronger in these defects compared to the flat surface.

This is seen also in Figure 6.4 where the energy distribution for the scratched surface extends longer in the lower energy region (corresponding to higher adsorption energies). It is further seen that the scratched surface have a wider distribution also for lower adsorption energies, corresponding to the positions adjacent to the scratches. This is probably due to how the defect surface was defined, with the scratches quite close to each other (see Figure 6.2). For a larger surface with flat areas between the scratches one would expect a distribution close to the one for the completely flat surface, but with a tail towards higher adsorption energies corresponding to the positions within the scratches.
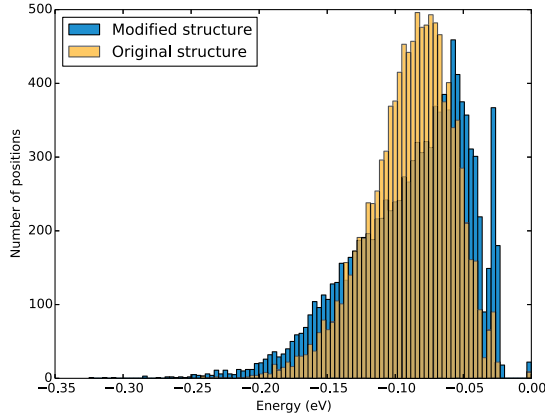

Figure 6.4. Distribution of the minimum energy values shown in Figure 6.3 for the flat (original), and the scratched (modified) surface.

6.2.4 Diffusion coefficients

The dynamics of atoms adsorbed onto a surface may be studied by looking at the surface diffusion coefficient for the adsorbent on the surface [75, 76]. We assume that the desorption rate from a surface increases if the adsorbed atoms can move over the surface more easily, in order to reach a position where the desorption energy is low. The desorption rate is thus dependent on the surface diffusion coefficient, which is why this part of the study was performed.

The diffusion coefficient can be expressed in terms of the velocity autocorrelation functions of the atoms:

$$D = \lim_{t \to \infty} \frac{\langle (\vec{r}(t) - \vec{r}(0))^2 \rangle}{6t} = \frac{1}{3} \int_0^\infty \langle \vec{v}(t) \cdot \vec{v}(0) \rangle dt \qquad (6.9)$$

This is a well known relation by Einstein, which can be found in various textbooks on molecular dynamics [64, 77, 63]. This relation is valid for a system in equilibrium, and the average is to be calculated as an ensemble average.

The expression can be further divided into a parallel part and a perpendicular part, with respect to the surface under study [75, 76], and an expression for the surface diffusion coefficient D_S may be obtained:

$$D_S = \int_0^\infty \frac{1}{2} \langle (v_x(t)v_x(0) + v_y(t)v_y(0)) \rangle dt \qquad (6.10)$$

Equation 6.10 describes surface diffusion for a surface in the xy-plane.

In Paper V the diffusion was studied by placing about 1300 Xe atoms on the surface, and then recording their trajectories for 4000 ps at a constant temperature of 100 K. In these simulations only the Xe-Al and the Xe-O interactions were considered, and the xenon atoms were thus independent from each other. When the system had reached equilibrium a series of velocity autocorrelation functions were calculated for 100 ps each and averaged over all Xe atoms. The resulting 3701 autocorrelation functions were then averaged in order to approximate the ensemble average. Finally, the surface diffusion coefficient was calculated by integrating the autocorrelation functions according to Equation 6.10.

This procedure was repeated for both the flat and the scratched surfaces and, as shown in Figure 7 in Paper V, the resulting autocorrelation functions oscillate around zero for large t and the diffusion coefficients approaches a finite value. The resulting diffusion coefficient is found to be 2.3 times lower for the scratched surface, than for the flat surface, which indicates that the xenon atoms are more likely to stay localized in the adsorption sites on the scratched surface, compared to the flat one. Despite this very simple model these findings offer a possible explanation to the need for unexpectedly thick ALD deposited Al_2O_3 films to significantly reduce the memory effect in the SAUNA plastic scintillator detector.

6.2.5 Discussion and conclusions

Three main conclusions can be drawn from the results presented in Sections 6.2.3 and 6.2.4.

The first is that, according to this study, it seems like xenon may be adsorbed to some extent onto an Al_2O_3 surface at room temperature.

Secondly, the adsorption energies are larger for the scratched surface than for the flat one, and finally, the surface diffusion is found to be slower on the scratched surface compared to the flat one.

One may assume that the likelihood for an adsorbed atom to be desorbed from the surface increases if it can move over the surface towards a site with a lower desorption energy. In that case a lower diffusion coefficient indicates a lower desorption rate.

For our system, a higher adsorption energy for the scratched surface, together with a lower diffusion coefficient indicates that xenon atoms are more strongly bound to the scratched surface, compared to the flat one. This may in

turn explain a more pronounced memory effect for a system containing surface imperfections, as was our hypothesis from the beginning.

The study presented in Paper V is performed using rather simple potentials to describe the xenon-Al_2O_3 system, which is why no attempt is made to evaluate the quantitative magnitude of surface adsorption as a mechanism responsible for the memory effect in coated samples. The geometry of the surface defects studied here are also just one example, and a more careful study of the real surfaces would be needed in order to make more realistic simulations.

But even with this simple model one may draw some qualitative conclusions regarding the behavior of the system, as discussed in this chapter.

7. Conclusions

In this thesis a solution to the memory effect problem in the SAUNA plastic scintillator detectors, used for verification of the CTBT, has been proposed and demonstrated. The solution consists in coating the plastic scintillator detector with 425 nm Al_2O_3 using Atomic Layer Deposition. This coating has been shown to reduce the memory effect by a factor of 1000 compared to uncoated detectors.

Light collection simulations showed that if a smooth coating is achieved, with a refractive index close to the one of the plastic scintillator, the energy resolution of the detector should not be impaired. The simulations also showed that if a smooth coating is achieved on a rough detector surface, the light collection may even be improved by the coating. It was further seen through AFM pictures that the coating does have a smoothening effect on the plastic surface.

Measurements using the complete coated detector also resulted in an energy resolution comparable to uncoated detectors. However, since the resolution measurement was only performed on one detector, and since it is difficult to perform a reproducible measurement of the resolution before and after coating, it is difficult to draw any conclusions on the effect of the coating on the resolution from this measurement. The resolution has been shown to vary between individual detectors, depending on the quality of the plastic scintillator, and it is not clear how this particular one would have performed without the coating.

Currently the reproducibility and long term performance of the approach is investigated, and the coating procedure improved. This is done by FOI and the system manufacturer Scienta SAUNA systems, in collaboration with the coating company Nanexa AB. The plan is to introduce the coated detectors in the SAUNA systems that are part of the IMS network, once long term stability of the coating has been achieved.

The fact that the energy resolution does not seem to be impaired by the coating, but could even be improved, is something that may also be of interest for other detector applications, as was discussed in Section 5.6.

The coating of 425 nm needed to achieve the large memory effect reduction is rather thick. This could be explained by incomplete coverage of the plastic surface due to its hydrophobicity. Another potential explanation may be that the detector surface contains large defects in the form of scratches which may not be completely filled by the thinner coatings, resulting in adsorption sites in imperfections on the Al_2O_3 surface. This hypothesis was studied and supported by initial molecular dynamics simulations of the xenon-Al_2O_3 system.

This mechanism might be responsible for elevated memory effect with thinner films, in combination with incomplete coverage.

The diffusion mechanism behind the memory effect was also studied, strengthening the general hypothesis that diffusion is in fact the mechanism behind the memory effect. It was also found that saturation of the detector material with stable xenon does not remove the memory effect. This is believed to be due to significant exchange of xenon atoms at the surface through adsorption and desorption.

In addition to the study of metallic oxide coatings, in particular Al_2O_3, a theoretical study of graphene as a diffusion barrier for this application was conducted. The results showed, that from a theoretical point of view, even a graphene sheet containing large defects in the form of rips may work as a diffusion barrier in this application.

8. Summary of papers

Below follows a short summary of each of the papers included in this thesis, as well as my contribution to each paper.

Paper I: Investigations of surface coatings to reduce memory effect in plastic scintillator detectors used for radioxenon detection

This paper describes measurements conducted in order to identify a suitable coating that may be used to reduce the memory effect in the SAUNA plastic scintillator detectors. Al_2O_3 and SiO_2 coatings were deposited onto flat plastic scintillator samples, exposed to radioactive xenon, and the resulting memory effect in the samples were measured. The results showed that 425 nm of Al_2O_3 was a good candidate for further investigation.

My contribution:

I assembled the experimental setup used for the measurements at FOI, performed the measurements, and analyzed the results. I also participated in the measurements conducted at UT. I wrote the major part of the paper and had the main responsibility for its completion.

Paper II: Effects of surface coatings on the light collection in plastic scintillators used for radioxenon detection

This paper describes Monte Carlo simulations, as well as measurements, performed in order to evaluate the effect a surface coating would have on the light collection, and energy resolution, of the plastic scintillator detector in the SAUNA system. The effect was evaluated as a function of surface roughness, as well as thickness, and refractive index of the coating.

My contribution:

I performed all simulations and measurements, and analyzed the results. I also wrote the paper.

Paper III: Memory effect, resolution and efficiency measurements of an Al_2O_3 coated plastic scintillator used for radioxenon detection

This paper describes measurements with a complete SAUNA plastic scintillator detector coated with 425 nm Al_2O_3. The performance of this detector was evaluated in terms of memory effect, resolution and efficiency. The detector was found to have comparable resolution and efficiency to uncoated detectors, and the memory effect was reduced by a factor of 1000 by the coating.

My contribution:
I did the major part of the measurements and analysis of the results, and wrote the paper.

Paper IV: Assisted self-healing in ripped graphene
This paper describes a DFT study of the xenon diffusion barrier properties of a ripped graphene sheet.

My contribution:
I participated in the analysis of the results, and also took part in writing the paper.

Paper V: Molecular dynamics study of Xenon on an amorphous Al_2O_3 surface
This paper describes molecular dynamics simulations performed to investigate if xenon may be adsorbed on the Al_2O_3-surface, and if surface imperfections might cause an increased memory effect.

My contribution:
I performed a large part of the simulations and analysis of the results. I wrote the major part of the paper.

Acknowledgements

There are many people who have contributed to my work the past years and who have helped me move forward in one way or another.

First of all I would like to thank my supervisors Mattias Klintenberg, Henrik Sjöstrand and Anders Ringbom. You have all taught me a lot and been a great support throughout these years.

Thank you Mattias for your encouragement and enthusiasm, for all the opportunities and good advice you have given me, and for teaching me about modeling materials.

Thank you Henrik for being a good friend, for your interest, thoroughness, and all our discussions which have made my work better and more fun.

Anders, thank you for guiding me through the field of radioxenon detection, and for letting me travel the world.

I also want to give a big thank you to everyone at FOI for introducing me to an interesting field as well as for welcoming me to an inspiring workplace. In particular I would like to thank Klas Elmgren, Lars Mårtensson, Fredrik Nielsen, Mattias Aldener, Jenny Petersson, Lars-Erik de Geer and Hans Henriksson for helping me at different stages in the project, with everything from bending gas tubes to data analysis. A special thanks to Tomas Fritioff for helping me out in the lab, for always having time for discussions and for being so positive.

To my colleagues in the Materials Theory group, thank you all for giving me a pleasant workplace and for all the fika. I will probably never in my life eat as much princesstårta again. A special thanks to Oscar, Peter, Henrik, Annica, Anders, Kristofer and Jonas for nice lunches, coffee/fruit breaks and beer nights. Thank you Anna for being a great office mate.

I also want to thank everyone at the Division of Applied Nuclear Physics for fun coffee breaks, good collaboration on courses, and for including me in your after works and other events. Thanks to Matthias Weiszflog and Cecilia Gustavsson for taking me on as a course assistant. I really enjoyed working with you both and to help putting together the course.

To Steve Biegalski and Alex Fay at UT Austin, thank you for a great collaboration. I really enjoyed the time I got to spend with you in Austin.

Thanks also to Artur Tamm and Erki Metsanurk for collaborating on the MD paper, to Mats Boman and Indrek Jogi for helping with the first Al_2O_3

coatings, to Mårten Rooth at Nanexa for a good collaboration, and for answering all my ALD questions, to Arne Roos and Andreas Jonsson for letting me use their optical equipment, and to everyone at Scienta SAUNA systems for sharing their experience.

I would also like to thank Prof. Kai Vetter and Jonathan Maltz for welcoming me to UC Berkeley and LBL, and for teaching me new things outside my normal field. Last spring was a very valuable experience for me.

Thanks to all my friends and family that are spread all over the country and the world, for being part of my life outside the PhD work. The past years would not have been nearly as fun without you.

I want to give a special thank you to my parents for always believing in me and supporting me. To my dad for always giving good advice in times of need and to my mom for always being so interested in what I do. Thank you Mårten and Fabian for being great brothers, Ulla and Björn for all the blueberries, and my grandmother for much needed summer breaks in Osby.

Most of all, I want to thank Petter. For always being on my side and for believing in me no matter what. For encouraging me to take on challenges, for seeing possibilities in everything, and for being my best friend. I love you and I can't wait for our next adventure!

Sammanfattning

Det fullständiga provstoppsavtalet (CTBT) är ett internationellt avtal som förbjuder alla typer av kärnvapenprovsprängningar. Avtalet har skrivits på av de flesta av världens länder, men det fattas fortfarande några underskrifter innan det träder i kraft. När det gör det är det dock viktigt att det går att kontrollera att avtalet efterföljs. På grund av detta håller man just nu på att sätta upp ett internationellt nätverk av mätstationer (IMS), som har till syfte att detektera energin som frigörs i en kärnexplosion, samt de radioaktiva ämnen som skapas. När nätverket är färdigt kommer det att bestå av fler än 300 mätstationer som är utspridda över hela jordklotet.

Den frigjorda energin mäts i form av seismiska vågor i marken, hydroakustiska vågor i haven eller infraljudvågor i luften. För att kunna särskilja en kärnexplosion från en konventionell explosion är det viktigt att man också upptäcker en del av de radioaktiva ämnen som skapas i explosionen.

De flesta provsprängningar som har ägt rum under de senaste årtiondena har gjorts i underjorden, och i dessa fall stannar det mesta av radioaktiviteten kvar i hålrummet som blir till av explosionen. En del av de radioaktiva ämnena är dock i form av ädelgaser, till exempel xenon.

Ädelgaser reagerar inte gärna med andra ämnen, vilket gör att det är ganska stor sannolikhet att de kan sippra upp ur jorden, eller släppas ut ifall man skulle öppna upp hålrummet där explosionen ägde rum. På grund av detta använder man xenondetektionssystem som en del av IMS. Dessa har till syfte att fånga upp och mäta mängden av radioaktivt xenon i luften, och när nätverket är färdigt kommer det att finnas 40 sådana system utspridda över jorden.

Har man mätt förhöjda mängder av radioaktivt xenon på en viss plats, kan man sedan med hjälp av data om hur vindar har blåst ta reda på var detta xenon skulle kunna komma ifrån och på så sätt ta reda på ifall utsläppet skulle kunna vara från en kärnvapenexplosion.

En typ av xenondetektionssystem som används i IMS är SAUNA-systemet, som har utvecklats på FOI i Sverige. Detta system samlar in stora mängder luft, extraherar ett xenonprov från luften, och mäter sedan aktiviteten av xenonet i provet. Det radioaktiva xenonet sönderfaller och sänder i den processen ut strålning i form av fotoner eller elektroner. SAUNA-systemet innehåller en cylindisk ihålig detektorcell som fungerar både som en behållare för gasprovet under mätningen, och mäter strålningen som skickas ut då xenonet sönderfaller.

Ett problem med denna uppställning är att en del av xenonet diffunderar in och fastnar i detektormaterialet under mätningen. Detta innebär att när

man tömmer detektorcellen för att förbereda för nästa prov så har man kvar lite radioaktivt xenon i själva detektorn. Denna så kallade minneseffekt minskar systemets känslighet och försämrar kommande mätningar. Det är viktigt att mätsystemen i IMS är extremt känsliga eftersom xenonet kan ha färdats långa sträckor och spätts ut innan det når en mätstation. Minneseffekten är ett särskilt stort problem för mätstationer som står placerade i närheten av andra xenon-källor såsom kärnkraftverk eller fabriker som tillverkar radioaktiva isotoper.

Arbetet presenterat i den här avhandlingen har syftat till att hitta en lösning på det här problemet, för att förbättra xenondetektionen i IMS och göra det sannolikare att man kan upptäcka en hemlig kärnvapenprovsprängning.

En lösning som vi här har visat förminskar minneseffekten med en faktor 1000, är att belägga detektorcellen med Al_2O_3. Beläggningen har gjorts med tekninken ALD, som kan skapa mycket tunna filmer genom att lägga ett atomlager i taget av ett material på ytan man vill täcka. Al_2O_3 har visat sig effektivt stoppa xenon från att fastna i detektorn, utan att försämra detektorns prestanda.

Den största delen av mitt arbete har inneburit att testa hur bra olika typer av beläggningar stoppar xenonet från att fastna i detektormaterialet, samt att studera hur en beläggning påverkar ljustransporten i detektor. Det senare är viktigt då detektorn reagerar på strålningen genom att generera ljus. Detta ljus måste sedan samlas in och omvandlas till en elektrisk signal för att kunna analyseras. Detektorns energiupplösning beror på hur effektivt ljuset samlas in och en beläggning som till exempel absorberar en stor del av ljuset skulle kunna försämra mätningarna avsevärt. Det har dock visat sig att med en genomskinlig och slät beläggning, vilket Al_2O_3 är, så bör inte detta vara ett problem.

References

[1] K. S. Krane, *Introductory nuclear physics*. John Wiley & Sons, 1988.

[2] G. F. Knoll, *Radiation Detection and Measurement*. John Wiley & Sons, fourth ed., 2010.

[3] "http://physics.nist.gov/physrefdata/star/text/estar.html."

[4] G. F. Knoll, *Radiation Detection and Measurement*. John Wiley & Sons, third ed., 2000.

[5] S. Shionoya and W. M. Yen, *Phosphor Handbook*. CRC Press LCC, 1998.

[6] J. B. Birks, *The Theory and Practice of Scintillation Counting*. Pergamon Press Ltd., first ed., 1964.

[7] T. Jonter, "Nuclear non-proliferation - a brief historical background," in *Nuclear Safeguards and Non-Proliferation* (G. Janssens-Maenhout, ed.), 2008.

[8] "http://www.iaea.org/about/history.html."

[9] "www.ctbto.org/."

[10] "www.un.org/disarmament/WMD/nuclear/npt.shtml."

[11] A. Ringbom, "Nuclear treaty verification at FOI, annual report 2008," Tech. Rep. FOI-R-2790–SE, Swedish Defence Research Agency, FOI, 2009.

[12] M. Auer, A. Axelsson, X. Blanchard, T. W. Bowyer, G. Brachet, I. Bulowski, Y. Dubasov, K. Elmgren, J. P. Fontaine, W. Harms, J. C. Hayes, T. R. Heimbigner, J. I. McIntyre, M. E. Panisko, Y. Popov, A. Ringbom, H. Sartorius, S. Schmid, J. Schulze, C. Schlosser, T. Taffary, W. Weiss, and B. Wernsperger, "Intercomparison experiments of systems for the measurement of xenon radionuclides in the atmosphere," *Applied Radiation and Isotopes*, vol. 60, pp. 863–877, 2004.

[13] Y. V. Dubasov, Y. S. Popov, V. V. Prelovskii, A. Y. Donets, N. M. Kazarinov, V. V. Mishurinskii, V. Y. Popov, Y. M. Rykov, and N. V. Skirda, "The APIKC-01 automatic facility for measuring concentrations of radioactive xenon isotopes in the atmosphere," *Instruments and Experimental Techniques*, vol. 48, no. 3, pp. 108–114, 2005.

[14] P. L. Reeder, T. W. Bowyer, and R. W. Perkins, "Beta-gamma counting system for Xe fission products," *Journal of Radioanalytical and Nuclear Chemistry*, vol. 235, no. 1–2, pp. 89–94, 1998.

[15] A. Ringbom, T. Larsson, A. Axelsson, K. Elmgren, and C. Johansson, "SAUNA - a system for automatic sampling, processing, and analysis of radioactive xenon," *Nuclear Instruments and Methods in Physics Research A*, vol. 508, no. 3, pp. 542–553, 2003.

[16] J.-P. Fontaine, F. Pointurier, X. Blanchard, and T. Taffary, "Atmospheric xenon radioactive isotope monitoring," *Journal of Environmental Radioactivity*, vol. 72, pp. 129–135, 2004.

[17] C. R. Carrigan, R. A. Heinle, G. B. Hudson, J. J. Nitao, and J. J. Zucca, "Trace gas emissions on geological faults as indicators for underground nuclear testing," *Nature*, vol. 382, pp. 528–531, Aug 1996.

[18] T. W. Bowyer, C. Schlosser, K. H. Abel, M. Auer, J. C. Hayes, T. R. Heimbigner, J. I. McIntyre, M. E. Panisko, P. L. Reeder, H. Satorius, J. Schulze, and W. Weiss, "Detection and analysis of xenon isotopes for the comprehensive nuclear-test-ban treaty international monitoring system," *Journal of Environmental Radioactivity*, vol. 59, pp. 139–151, 2002.

[19] A. Axelsson, L. Mårtensson, A. Mörtsell, and A. Ringbom, "Improvement of the SAUNA noble gas system calibration procedures," Tech. Rep. FOI-R–3451–SE, Swedish Defence Research Agency, FOI, 2012.

[20] A. Ringbom, "Calculation of electron-photon coincidence decay if ^{131m}xe and ^{133m}xe including atomic relaxation," *Applied Radiation and Isotopes*, vol. 70, pp. 1499–1508, 2012.

[21] M. Auer, T. Kumberg, H. Sartorius, B. Wernsberger, and C. Schlosser, "Ten years of development of equipment for measurement of atmospheric radioactive xenon for the verification of the CTBT," *Pure and Applied Geophysics*, vol. 167, pp. 471–486, 2010.

[22] P. L. reeder, T. W. Bowyer, J. I. McIntyre, W. K. Pitts, A. Ringbom, and C. Johansson, "Gain calibration of a β/γ coincidence spectrometer for automated radioxenon analysis," *Nuclear Instruments and Methods in Physics Research A*, vol. 521, pp. 586–599, 2004.

[23] A. Axelsson and A. Ringbom, "Xenon air activity concentration analysis from coincidence data," Tech. Rep. FOI-R–0913–SE, Swedish Defence Research Agency, FOI, 2003.

[24] L.-E. D. Geer, "The xenon NCC method revisited," Tech. Rep. FOI-R–2350-SE, Swedish Defence Research Agency, FOI, 2007.

[25] "www.saunasystems.se/."

[26] R. W. Perkins and L. A. Casey, "Radioxenons: their role in monitoring a comprehensive test ban," Tech. Rep. DOE/RL-96-51; PNNL-SA–27750, Pacific Northwest National Laboratory, PNNL, 1996.

[27] M. B. Kalinowski and C. Pistner, "Isotopic signature of atmospheric xenon released from light water reactors," *Journal of Environmental Radioactivity*, vol. 88, pp. 215–235, 2006.

[28] P. R. J. Saey, T. W. Bowyer, and A. Ringbom, "Isotopic noble gas signatures released from medical isotope production facilities - simulations and measurements," *Applied Radiation and Isotopes*, vol. 68, pp. 1846–1854, 2010.

[29] M. B. Kalinowski, A. Axelsson, M. Bean, X. Blanchard, T. W. Bowyer, G. Brachet, S. Hebel, J. I. McIntyre, J. Peters, C. Pistner, M. Raith, A. Ringbom, P. R. J. Saey, C. Schlosser, T. J. Stocki, T. Taffary, and R. K. Ungar, "Discrimination of nuclear explosions against civilian sources based on atmospheric xenon isotopic activity ratios," *Pure and Applied Gephysics*, vol. 167, pp. 517–539, 2010.

[30] P. R. J. Saey, M. Bean, A. Becker, J. Coyne, R. d' Armours, L.-E. D. Geer, R. Hogue, T. J. Stocki, R. K. Ungar, and G. Wotawa, "A long distance measurement of radioxenon in Yellowknife, Canada, in late october 2006," *Geophysical Research Letters*, vol. 34, p. L20802, 2007.

[31] A. Ringbom, K. Elmgren, K. Lindh, J. Peterson, T. W. Bowyer, J. C. Hayes, J. I. McIntyre, M. Panisko, and R. Williams, "Measurements of radioxenon in

ground level air in South Korea following the claimed nuclear test in North Korea," *Journal of Radioanalytical Chemistry*, vol. 282, pp. 773–779, 2009.

[32] A. Ringbom, A. Axelsson, M. Aldener, M. Auer, T. W. Bowyer, T. Fritioff, I. Hoffman, K. Khrustalev, M. Nikkinen, V. Popov, Y. Popov, K. Ungar, and G. Wotawa, "Radioxenon detections in the CTBT international monitoring system likely related to the announced nuclear test in North Korea on February 12, 2013," *Journal of Environmental Radioactivity*, vol. 128, pp. 47–63, 2014.

[33] M. Bean, N. St-Amant, and R. K. Ungar, "Understanding the memory effect in SAUNA's plastic scintillator and its impact on the measurement, poster presented at noble gas workshop in nevada, USA," Nov 2007.

[34] J. I. McIntyre, K. H. Abel, T. W. Bowyer, J. C. Hayes, T. R. Heimbigner, M. E. Panisko, P. L. Reeder, and R. C. Thompson, "Measurements of ambient radioxenon levels using the automated radioxenon sampler/analyzer (ARSA)," *Journal of Radioanalytical and Nuclear Chemistry*, vol. 248, no. 3, pp. 629–635, 2001.

[35] B. D. Milbrath, M. W. Cooper, L. S. Lidey, T. W. Bowyer, J. C. Hayes, J. I. McIntyre, L. Karr, D. Shafer, and J. Tappen, "Radioxenon atmospheric measurements in north Las Vegas, NV," in *29th Monitoring Research Review: Ground-Based Nuclear Explosion Monitoring Technologies*, 2007.

[36] L. A. Currie, "Limits for qualitative detection and quantitative determination," *Analytical Chemistry*, vol. 40, p. 586, 1968.

[37] C. E. Seifert, J. I. McIntyre, K. C. Antolick, A. J. Carman, M. W. Cooper, J. C. Hayes, T. R. Heimbigner, C. W. Hubbard, K. E. Litke, M. D. Ripplinger, and R. Suarez, "Mitigation of memory effects in beta scintillation cells for radioactive gas detection," in *27th Seismic Research Review: Ground-Based Nuclear Explosion Monitoring Technologies*, 2005.

[38] "http://www.detectors.saint-gobain.com/uploadedfiles/sgdetectors/documents/product_data_sheets/bc400-404-408-412-416-data-sheet.pdf."

[39] H. Chatham, "Oxygen diffusion barrier properties of transport oxide coatings on polymeric substrates," *Surface and Coatings Technology*, vol. 78, pp. 1–9, 1994.

[40] M. D. Groner, S. M. George, R. S. McLean, and P. F. Garcia, "Gas diffusion barriers on polymers using Al_2O_3 atomic layer deposition," *Applied Physics Letters*, vol. 88, p. 051907, 2006.

[41] R. L. Puurunen, "Surface chemistry of atomic layer deposition: A case study for the trimethylaluminum/water process," *Journal of Applied Physics*, vol. 97, 2005.

[42] M. D. Groner, F. H. Fabreguette, J. W. Elam, and S. M. George, "Low-temperature Al_2O_3 atomic layer deposition," *Chemistry of Materials*, vol. 16, pp. 639–645, 2004.

[43] J. L. Vossen and W. Kern, eds., *Thin Film Processes II*. Elsevier, 1991.

[44] A. Fay, "Mitigation of the radioxenon memory effect in beta-gamma detector systems by deposition of thin film diffusion barriers on plastic scintillator," Master's thesis, University of Texas at Austin, 2010.

[45] S. A. Stern and J. R. Fried, "Permeability of polymers to gases and vapors," in *Physical properties of polymers handbook*, Springer New York, 2007.

[46] J. G. Wijmans and R. W. Baker, "The solution-diffusion model: a review," *Journal of membrane science*, vol. 107, pp. 1–21, 1995.

[47] D. L. Beke, ed., *Diffusion in Non-Metalllic Solids (Part 1)*, vol. 33B1 of *Landolt-Börnstein - Group III Condensed Matter*. Springer Berlin Heidelberg, 1999.

[48] S. C. George and S. Thomas, "Transport phenomena through polymeric systems," *Progress in Polymer Science*, vol. 26, pp. 985–1017, 2001.

[49] E. Sada, H. Kumazawa, H. Yakushiji, Y. Bamba, K. Sakata, and S.-T. Wang, "Sorption and diffusion of gases in glassy polymers," *Industrial Engineering and Chemistry Research*, vol. 26, pp. 433–438, 1987.

[50] C. Kittel and H. Kroemer, *Thermal Physics*. W. H. Freeman Co Ltd, second ed., 1980.

[51] A. Thran, G. Kroll, and F. Faupel, "Correlation between fractional free volume and diffusivity of gas molecules in glassy polymers," *Journal of Polymer Science*, vol. 37, pp. 3344–3358, 1999.

[52] H. Sjöstrand, E. A. Sunden, A. Conroy, G. Ericsson, M. G. Johnsson, L. Giacomelli, G. Gorini, C. Hellesen, A. Hjalmarsson, S. Popovichev, E. Ronchi, M. Tardocchi, M. Weiszflog, and J. Contributors, "Gain stabilization control system of the upgraded magnetic proton recoil neutron spectrometer at JET," *Review of Scientific Instruments*, vol. 80, p. 063505, 2009.

[53] C. Moisan, F. Cayouet, and G. McDonald, *DETECT2000 The Object Oriented C++ Language Version of DETECT A Program for Modeling Optical Properties of Scintillators*, 2000.

[54] G. Binnig and C. F. Quate, "Atomic force microcope," *Physical Review Letters*, vol. 56, pp. 930–933, 1986.

[55] "Personal communication with tomas fritioff at foi in december 2013."

[56] J. S. Bunch, S. S. Verbridge, J. S. Alden, A. M. van der Zande, J. M. Parpia, H. G. Craighead, and P. L. McEuen, "Impermeable atomic membranes from graphene sheets," *Nano Letters*, vol. 8, pp. 2458–2462, 2008.

[57] P. Hohenberg and W. Kohn, "Inhomogeneous electron gas," *Physical Review*, vol. 136, p. B864, 1964.

[58] W. Kohn and L. J. Sham, "Self-consistent equations including exchange and correlation effects," *Physical Review*, vol. 140, p. A1133, 1965.

[59] P. Koskinen, S. Maola, and H. Häkkinen, "Self-passivating edge reconstructions of graphene," *Physical Review Letters*, vol. 101, p. 115502, 2008.

[60] B. W. Sturm, N. J. Cherepy, O. B. Drury, P. A. Thelin, S. E. Fisher, S. A. Payne, A. Burger, L. A. Boatner, J. O. Ramey, K. S. Shah, and R. Hawrami, "Effects of packaging sri$_2$(eu) scintillator crystals," *Nuclear Instruments and Methods in Physics Research A*, vol. 652, pp. 242–246, 2011.

[61] N. J. Cherepy, G. Hull, A. D. Drobshoff, S. A. Payne, E. van Loef, C. M. Wilson, K. S. Shah, U. N. Roy, A. Burger, L. A. Boatner, W.-S. Choong, and W. W. Moses, "Strontium and barium iodide high light yield scintillators," *Apllied Physics Letters*, vol. 92, p. 083508, 2008.

[62] K. S. Shah, J. Glodo, M. Klugerman, L. Cirignano, W. W. Moses, S. E. Derenzo, and M. J. Weber, "LaCl$_3$:Ce scintillator for γ-ray detection," *Nuclear Instruments and Methods in Physics Research A*, vol. 505, pp. 76–81, 2003.

[63] J. M. Haile, *Molecular Dynamics Simulation, Elementary methods*. John Wiley & Sons, 1992.

[64] A. R. Leach, *Molecula Modeling, Principles and Applications*. Pearson Education Limited, second ed., 2001.

[65] R. Petrenko and J. Meller, "Molecular dynamics," in *Encyclopedia of Life Sciences*, John Wiley & Sons, 2010.

[66] C. Kittel, *Introduction to Solid State Physics*. John Wiley & Sons, eigth ed., 2005.

[67] M. Matsui, "A transferable interatomic potential model for crystals and melts in the system CaO-MgO-Al_2O_3-SiO_2," *Mineralogical Magazine*, vol. 58A, pp. 571–572, 1994.

[68] G. Gutierrez, A. B. Belonoshko, R. Ahuja, and B. Johansson, "Structural properties of liquid Al_2O_3: A molecular dynamics study," *Physical Review E*, vol. 61, no. 3, p. 2723, 2000.

[69] G. Gutierrez and B. Johansson, "Molecular dynamics properties of amorphous Al_2O_3," *Physical Review B*, vol. 65, p. 104202, 2002.

[70] E. A. Chagarov and A. C. Kummel, "Generation of realistic amorphous Al_2O_3 and ZrO_2 samples by hybrid classical and first principle molecular dynamics simulations," *ECS Transactions*, vol. 16, pp. 773–785, 2008.

[71] S. P. Adiga, P. Zapol, and L. A. Curtiss, "Atomistic simulations of amorphous alumina surfaces," *Physical Review B*, vol. 74, p. 064204, 2006.

[72] "http://lammps.sandia.gov."

[73] S. Plimpton, "Fast parallel algorithms for short-range molecular dynamics," *Journal of Computational Physics*, vol. 117, pp. 1–19, 1995.

[74] H. Momida, T. Hamada, and Y. Takagi, "Theoretical study on dielectric response of amorphous alumina," *Physical Review B*, vol. 73, p. 054104, 2006.

[75] J. L. Ricccardo and W. A. Steeke, "Molecular dynamics study of tracer diffusion of argon adsorbed on amorphous surfaces," *The Journal of Chemical Physics*, vol. 105, p. 9674, 1996.

[76] J. M. Stallons and E. Iglesia, "Simulations of the structure and properties of amorphous silica surfaces," *Chemical Engineering Science*, vol. 56, pp. 4205–4216, 2001.

[77] M. P. Allen and D. J. Tildesley, *Computer Simulation of Liquids*. Clarendon Press, Oxford, 1987.

[78] "http://www.graphene.manchester.ac.uk/story/properties/."

[79] A. Hinchliffe, *Molecular modelling for beginners*. John Wiley & Sons, 2003.

[80] V. V. Hoang, "Molecular dynamics study on structure and properties of liquid and amorphous Al_2O_3," *Physical Review B*, vol. 70, p. 134204, 2004.

[81] "http://www.iaea.org/newscenter/focus/npt/index.shtml."

[82] O. Leenaerts, B. Partoens, and F. M. Peeters, "Graphene: A perfect nanoballoon," *Applied Physics Letters*, vol. 93, p. 193107, 2008.

[83] "http://www.un.org/disarmament/WMD/nuclear/npttext.shtml."

[84] "www.nucleide.org."

[85] V. P. Verma, S. Das, I. Lahiri, and W. Choi, "Large-area graphene on polymer film for flexible and transparent anode in field emission device," *Applied Physics Letters*, vol. 96, p. 203108, 2010.

Acta Universitatis Upsaliensis

Digital Comprehensive Summaries of Uppsala Dissertations
from the Faculty of Science and Technology 1111

Editor: The Dean of the Faculty of Science and Technology